NEW HYPOTHESIS FOR VULNERABLE PLAQUE RUPTURE DUE TO MICROCALCIFICATIONS IN THIN FIBROUS CAPS

by

Yuliya Vengrenyuk

A dissertation submitted to the Graduate Faculty in Engineering

in partial fulfillment of the requirements for the degree of

Doctor of Philosophy, The City University of New York

2009

This manuscript has been read and accepted for the
Graduate Faculty in Engineering in satisfaction of the
dissertation requirement for the degree of Doctor of Philosophy

_____	_____
Date	Dr. Sheldon Weinbaum Chair of Examining Committee
_____	_____
Date	Dr. Mumtaz Kassir Executive Officer

Dr. Stephen C. Cowin _____

Dr. Mitchell B. Schaffler _____

Dr. Luis Cardoso _____

Dr. Gwendalyn J. Randolph _____

THE CITY UNIVERSITY OF NEW YORK

Abstract

NEW HYPOTHESIS FOR VULNERABLE PLAQUE RUPTURE

DUE TO MICROCALCIFICATIONS IN THIN FIBROUS CAPS

by

Yuliya Vengrenyuk

Adviser: Professor Sheldon Weinbaum

Co-mentors: Professor Stephen C. Cowin, Professor Mitchell B. Schaffler, Professor Luis Cardoso, and Professor Gwendalyn J. Randolph

This dissertation develops a new paradigm for the rupture of thin-cap fibroatheroma (TCFA), namely that minute (10-20 μm-diameter) cellular-level microcalcifications in the cap proper can cause local stress concentrations around these minute spherical inclusions that lead to cavitation induced interfacial debonding and rupture. The hypothesized rigid inclusions, which lie below the visibility of current *in vivo* imaging techniques, are detected herein for the first time in fibrous caps of human coronary lesions. First, I develop a three-dimensional (3D) theoretical model of a perfectly bonded spherical inclusion in a fibrous cap and obtain an infinite series solution for the stress concentration around the hypothesized solid inclusion (Vengrenyuk *et al*., 2006). The model predicts a nearly twofold increase in peak circumferential stress (PCS)

at the inclusion interface which is sufficient to exceed the critical yield stress of the cap provided its thickness is < 65 μm in close agreement with the histological observations. Having demonstrated the quantitative feasibility of the hypothesis, I provide the first experimental evidence for the existence of these cellular-level microcalcifications in fibrous caps of autopsy specimens from human coronary lesions using confocal staining and micro-computed tomography (micro-CT) imaging techniques whose resolution far exceeds existing *in vivo* imaging methods. To further investigate the new paradigm for the rupture of TCFA, I develop a more sophisticated multi-level finite element model (FEM) of realistic 3D geometries of human coronary lesions based on high resolution micro-CT imaging (Vengrenyuk et al., 2008). The new model predicts that cellular-level calcifications by themselves may not be dangerous unless they lie in a region of high background stress. The most dangerous situations occur when 1) a microinclusion appears in close proximity to a region where the PCS is already high, 2) the microcalcification has an elongated shape, or 3) there are two microcalcifications in close proximity to one another. Finally, I apply histology based finite element analysis (FEA) to evaluate peak circumferential stresses in mouse aortic and brachiocephalic (BCA) lesions to test the hypothesis that these stresses are responsible for the greater stability of aortic lesions in mice. This analysis is able to both explain the greater stability of aortic lesions in mice and provide new insight into the BCA lesion as a model for the stability of human lesions with and without microcalcifications in their fibrous caps.

Acknowledgements

To my parents, my husband, and my sons for their love, patience, support, encouragement and belief in me

First and foremost I want to thank Dr. Sheldon Weinbaum, my PhD advisor and mentor, for his guidance, support and help with my research and life in general. I will always remember his words of wisdom and encouragement, his endless patience in reading my papers draft after draft. I will never stop to admire his creativity and magical insights. Thank you Dr. Weinbaum for helping me “to find my own voice”.

I am very grateful for having an exceptional doctoral committee and wish to thank Dr. Stephen C. Cowin, Dr. Mitchell B. Schaffler, Dr. Gwendalyn J. Randolph, and Dr. Luis Cardoso for their guidance over the years, continuous support and encouragement. I want to thank Dr. Cowin for support and advice, for many helpful discussions on the formulation of the theoretical model. I also want to thank Dr. Cowin for letting me participate in the preparation of the manuscript for the "Tissue Mechanics" book.

I would like to thank Dr. Randolph for her generosity to allow me to work in her lab for more than a year, for advising me in experimental work and paper writing. Dr. Randolph introduced me to the field of murine models for atherosclerosis which I’m planning to continue studying in the future. I greatly appreciate the help from all her students and postdocs, especially Theodore Kaplan, Lo Kuan, Emmanuel Gautier, and Stephane Potteaux.

I thank Dr. Schaffler for his advice, guidance, and for his generous access to the micro-CT facility at the Department of Orthopaedics at Mount Sinai School of Medicine. A large part of this work wouldn't have been completed without his help. I would like to acknowledge and thank Dr. Cardoso for giving me constant motivation and encouragement, for his help with micro-CT scanning, finite element techniques and basically with every other aspect of my research over the last three years. I'm very grateful for the opportunity to work in his lab. Many thanks to his PhD student Ian Gu for the support he has given me over all these years.

Very special thanks to Dr. Fritton for her help and care as a PhD students adviser, Dr. Ganatos for helping me with the analytical solution, and Dr. Gilchrist for teaching confocal microscopy. I would like to take this opportunity to thank Dr. Virmani and Dr. Kolodgie from CVPathology lab, MD for providing access to autopsy specimens for confocal imaging; Dr. Carlier from Columbia University for providing human coronary arteries for micro-CT scanning and for introducing me to the field of *in vivo* imaging techniques, OCT and IVUS.

I extend my many thanks to all former and current students from Dr. Weinbaum's lab: Dr. Qianhong Wu, Dr. Mia Thi, Dr. Xiaobing Zhang, Dr. Yuefeng Han, Dr. Yilin Wang, Dr. Yi Duan, Danielle Wu, Parisa Mirbod, Adreanne Kelly and Laura Causey. It's a great group of amazing people who feel like an extended family. Last but not least, a special thanks to Patricia Cupid and Carol Bamberger for their administrative help.

Table of Contents

List of Tables

Chapter 4

List of Figures

Chapter 2

Chapter 3

Chapter 4

Chapter 1 Introduction

In this dissertation I advance a new hypothesis for the rupture of vulnerable plaque due to the presence of minute (10-20 μm-diameter) cellular-level microcalcifications in the cap proper. The hypothesis suggests that these solid inclusions, which heretofore have gone undetected because they lie below the visibility of current in vivo imaging techniques, can cause local stress concentrations at the tissue/inclusion interface that lead to cavitation induced interfacial debonding and rupture.

Despite major advances in treatment of coronary heart disease patients, a large number of victims of the disease who are apparently healthy die suddenly without prior symptoms. Available screening and diagnostic techniques are insufficient to identify the victims before the event occurs. As a result, coronary heart disease remains the principal killer in the western world. Patients with acute coronary syndromes classically present with unstable angina, acute myocardial infarction, or sudden coronary death. More than half of the 500,000 coronary artery disease deaths every year are due to the sudden rupture of vulnerable plaque. It has been widely assumed that plaque morphology is the major determinant of clinical outcome (Little, 1990; Lendon *et al.,* 1991; Falk, 1992; Muller and Tofler, 1992; Libby 1995, 2001; Virmani *et al.,* 2000). Several pathological studies of ruptured plaques have provided morphological descriptions of the high-risk, or vulnerable, coronary plaque that is prone to rupture as a positively remodeled lesion rich in vasa-vasorum, containing a lipid-rich core with an overlying thin fibrous cap infiltrated by macrophages (Burke *et al*., 1997, 1999; Virmani *et al*., 2000; Maehara *et al*. 2002).

Virmani *et al.* (2003) described thin-cap fibroatheroma (TCFA) with a large necrotic core and a fibrous cap < 65 μm as a more specific precursor of plaque rupture due to tissue stress.

Despite the detailed analysis of plaque morphology in necropsy specimens from sudden death victims, the mechanism as to why some thin caps rupture and others do not has remained a mystery since ruptures often occur in regions where computational finite element (FE) and fluid structure interaction (FSI) models do not predict maximal stress. Forty percent of ruptures occur in the central part of the cap (Maehara *et al*., 2002) rather than regions of high curvature at the shoulders of the lipid core where FEM models predict maximum tissue stresses (Cheng *et al*., 1993). Similarly, the recent study by Tang *et al.* (2005) using an FSI model applied to 3D MRI images of sample plaques predicts that maximal stress often appears at healthy parts of the vessel where the vessel wall is thinner than the wall on the diseased plaque side or where vessel wall curvature is large. Our new hypothesis was conceived to explain these paradoxical observations and computational predictions.

At first glance, it might seem highly implausible that such minute inclusions are destabilizing when a series of FE models predict that much larger millimeter-size macrocalcifications, frequently observed in advanced human coronary lesions, have a stabilizing effect (Huang *et al*., 2001; Imoto *et al*., 2005). Our new hypothesis is inspired by the classical theoretical studies of Goodier (1933) who examined the effect of minute solid spherical impurities in rubber tires as a cause of their failure. Subsequent experiments by Gent and Park (1984) showed that debonding occurred at the interface between the solid impurity and rubber because of the large mismatch in hardness of the

materials and the local stress concentrations that develop at the poles of the impurity along the tensile axis as a result of this mismatch.

Since there were no prior reports of cellular-level solid inclusions in the fibrous caps of human coronary lesions, our initial effort was to explore the quantitative feasibility of the hypothesis to provide a framework for understanding the importance of the size of the hypothesized impurity and its location. In **Chapter 2** I will present a 3D model of a perfectly bonded rigid spherical inclusion in a fibrous cap under uniaxial tension which was constructed to predict the stress concentration around the inclusion. I will develop an analytical solution for the asymmetric problem, where the solid inclusion is arbitrarily positioned in the thickness direction. I find that there is a near doubling of the interface stress at the poles of the calcified inclusion and this doubling is only modestly affected by the positioning of the calcification within the cap thickness as shown. The model will provide a plausible explanation of the paradox that most plaque ruptures occur close to a region of high circumferential tensile stress, defined as a stress of more than 300kPa, but ruptures are not necessarily located at the points of maximum stress. I will also show that the results of this new analysis predict the critical cap thickness of 65 μm proposed by Virmani *et al.* (2003) for vulnerable plaque rupture.

Having demonstrated the quantitative feasibility of the new hypothesis, I explore *in vitro* imaging techniques whose resolution far exceed conventional MRI, IVUS and OCT approaches to confirm that the proposed solid inclusions do exist in fibrous caps of human atherosclerotic lesions. Cellular-level microcalcifications were considered the best candidates for the hypothesized weakening factors in the cap. This was suggested by the fact that macrophages and smooth muscle cells (SMCs) in the necrotic core were

observed to calcify after apoptosis. In addition, the presence of small cellular- and subcellular-level calcified inclusions in necrotic cores of advanced atherosclerotic lesions has been reported in a number of histological studies. However, there were no prior reports of cellular-level calcifications in the cap proper. First, I will examine autopsy specimens of coronary atheromatous lesions using confocal microscopy combined with calcium specific stain Alizarin Red S and present the first confocal images of microcalcifications in a fibrous cap of human fibroatheroma lesion. Then I will develop a non-destructive 3D approach for microcalcification detection using high resolution micro-CT imaging and show the first micro-CT images of spherical (≈ 20 micron diameter) microcalcifications in a thick-cap human atheroma lesion.

The first images of cellular-level calcifications in the cap proper clearly demonstrated that our original theoretical model of a spherical inclusion was too simplistic to predict their impact on plaque stability. Fist, the images showed that some microcalcifications are not spherical, but can take on elongated shapes and they can also have neighboring microcalcifications. Second, in any given FE calculation an accurate model is needed to determine the background stress in the cap. The majority of existing FEMs are based on 2D geometries of the lesion cross-sections obtained from histology, OCT, IVUS or MRI. Such a 2D computational approach wouldn't be sufficient to precisely define the PCS in lesions with complex geometries containing large mm-size macrocalcifications and cellular-size microcalcifications in the cap. To overcome these limitations, I will develop in **Chapter 3** a more realistic micro-CT based 3D FE approach which has the capability of predicting the stress distribution around an arbitrarily shaped micro-inclusion in a fibrous cap of a vulnerable plaque of arbitrary geometry. The

geometry of the plaque is reconstructed from high resolution micro-CT images of realistic human coronary lesions and similarly the shape of the microinclusions. Then, I will use the multi-level FE model of cellular-level microcalcifications in the cap proper to evaluate the effect of both micro and macro size calcific deposits described in Chapter 2 on the stress distribution in thin cap fibroatheromas. I analyze the impact of the shape of microcalcifications, their location and proximity to one another on biomechanical plaque stability.

Although numerous histopathology studies of postmortem human arteries summarized at the beginning of the Chapter have provided invaluable information about histological features of vulnerable plaque, these studies don't allow prospective examination of the events that lead to plaque rupture. It's generally accepted that there is an urgent need for a representative animal model where the rupture process itself can be predicted (Jackson *et al.* 2007). ApoE-deficient mice with diet induced lesions have been widely used to mimic many of the characteristics of human lesions including macrophage expression and the activity of MMPs. Recent studies summarized in **Chapter 4** have shown the feasibility of developing advanced lesions in the aorta and brachiocephalic arteries. These studies show that the remarkable feature of murine aortic lesions is that their fibrous caps are very thin, ≈ 10 micron, but they never appear to rupture despite the fact that the average systolic and diastolic pressures in these mice are 125 and 90 mmHg respectively, and thus not very different than humans. This observation is in marked contrast to the widely held belief that the thinner the cap the greater its instability and, therefore, is a paradox of great importance in understanding the mechanisms of plaque rupture. In Chapter 4 I will use histology based FEA to evaluate peak circumferential

stresses in aortic and BCA lesions from six fat fed ApoE KO mice. This analysis will be able to both explain the greater stability of aortic lesions in mice and provide new insight into the BCA lesion as a model for the stability of human lesions with and without microcalcifications in their fibrous caps. I find the average peak stress in fibrous caps of aortic lesions to be significantly lower than the average value of maximum stresses in BCA caps. I will also show that the proximal BCA artery of the fat-fed apoE knockout mouse is a better site to study pathophysiology of plaque rupture although they are too thin to contain cellular microcalcifications in the cap proper. Despite the absence of these microcalcifications the murine BCA lesions have stress levels that are quite similar to the PCS of the much thicker vulnerable caps of humans with such microcalcifications

Chapter 2 New hypothesis for vulnerable plaque rupture: stress induced debonding around cellular-level microcalcifications in thin fibrous caps

2.1 Introduction

The rupture of the thin fibrous cap overlying the necrotic core of a vulnerable plaque is the principal cause of acute coronary syndrome. It has been widely assumed that plaque morphology is the major determinant of clinical outcome (Little, 1990; Lendon *et al.,* 1991; Falk, 1992; Muller and Tofler, 1992; Virmani *et al.,* 2000). Several pathological studies of ruptured plaques have provided morphological descriptions of the high-risk, or vulnerable, coronary plaque that is prone to rupture or erosion as a positively remodeled lesion rich in vasa-vasorum, containing a lipid-rich core with an overlying thin fibrous cap infiltrated by macrophages (Burke *et al*., 1997, 1999; Virmani *et al*., 2000, 2003; Maehara *et al*., 2002). Virmani *et al.* (2003) described thin-cap fibroatheroma with a large necrotic core and a fibrous cap < 65 μm as a more specific precursor of plaque rupture due to tissue stress.

Despite the above observations, the mechanism of vulnerable plaque rupture has remained a mystery since ruptures often occur in regions where computational finite element (FEM) and fluid structure interaction (FSI) models do not predict maximal stress. Forty percent of ruptures occur in the central part of the cap rather than regions of high curvature at the shoulders of the lipid core where FEM models predict maximum tissue stresses (Cheng *et al*., 1993; Maehara *et al*. 2002). Similarly, the latest study by Tang *et al.* (2005) using an FSI model applied to 3D MRI images of sample plaques

predicts that maximal stress often appears at healthy parts of the vessel where the vessel wall is thinner than the wall on the diseased plaque side or where vessel wall curvature is large. Finally, millimeter size or larger calcifications beneath or adjacent to a lipid laden necrotic core, which can be easily observed by intravascular ultrasound (IVUS) or optical coherence tomography (OCT), have been theoretically predicted to be stabilizing (Huang *et al*., 2001; Imoto *et al*., 2005). Our new hypothesis was conceived to explain these paradoxical observations and computational predictions.

In this Chapter we propose a new hypothesis for the rupture of thin-cap fibroatheroma, namely that it is due to stress induced debonding of minute calcifications, the size of a single cell, whose mass is six or more orders of magnitude smaller than the millimeter or larger calcifications observed in MRI, IVUS and OCT mentioned previously. At first glance, it might seem highly implausible that such minute inclusions are destabilizing when FEM models predict, as noted earlier, much larger calcifications are stable (Huang *et al*., 2001; Imoto *et al*., 2005). Our new hypothesis is inspired by the classical theoretical studies of Goodier (1933) who examined the effect of minute solid spherical impurities in rubber tires as a cause of their failure. Subsequent experiments by Gent and Park (1984) showed that debonding occurred at the interface between the solid impurity and rubber because of the large mismatch in hardness of the materials and the local stress concentrations that develop at the poles of the impurity along the tensile axis as a result of this mismatch.

Goodier's classical analysis describes a small spherical impurity in an infinite medium. In the present study, we are interested in the case where the dimensions of the solid inclusion (10 μm) are a significant fraction of the cap thickness and where the

location of the impurity within the fibrous cap can be arbitrary. The problem we are interested in is basically that of a rigid spherical inclusion asymmetrically positioned in a thin elastic layer subject to uniaxial tension at infinity. This is a classical unsolved problem in the mechanics literature. The problem was of considerable interest in the 1970's when investigators were studying the fatigue fracture of high hardness steels with spherical inclusions or voids. The effect of a solid impurity near a free surface in a semi-infinite medium was first studied by Tsutsi and Saito (1973). Subsequently, Tsuchida and coworkers developed a solution for spherical voids in plates (1976) and then for a symmetrically located spherical solid inclusion of varying hardness (1979). The solutions for a spherical void showed large variation of stress concentration as a function of inclusion position suggesting that a similar behavior might occur for a solid inclusion. The asymmetric problem, where the solid inclusion is arbitrarily positioned in the thickness direction, is treated herein for the first time. Our solutions predict that there is a near doubling of the interface stress at the poles of the calcified inclusion and this doubling is only modestly affected by the positioning of the calcification within the cap thickness. Furthermore, the results of this new analysis predict, quite remarkably, the critical cap thickness of 65 μm proposed by Virmani *et al.* (2003) for vulnerable plaque rupture.

Having demonstrated the quantitative feasibility of our microcalcification hypothesis, we explored *in vitro* imaging techniques whose resolution far exceeded conventional MRI, IVUS and OCT approaches to confirm that the proposed cellular-level microcalcifications actually exist. To this end, we examined autopsy specimens of coronary atheromatous lesions using confocal microscopy combined with calcium

specific stains and micro CT imaging. At the end of the paper we present the first images of microcalcifications in fibrous caps. As anticipated, the minute inclusions in the cap are very rare compared to the numerous calcified macrophages observed in the necrotic core. The most likely candidates for the inclusions are either calcified smooth muscle cells or macrophages that have undergone apoptosis while crossing the cap in their migration into or out of the necrotic lipid core.

2.2 Methods

Fluorescent confocal imaging. Human coronary segments obtained at autopsy time, less than 12 hours after death were pressure fixed with 10% formalin and later stained with 2% aqueous solution of Alizarin Red S (SIGMA A5533-25G) at pH 4.2 for 5 minutes (Bernacca *et al.* 1994). After staining, the samples were washed twice with de-ionized H_2O followed by 70% ethanol to remove the excess stain from the tissue. The segments were examined using a confocal laser scanning microscope system Leica DM IRE2 with an oil immersed objective (index of refraction n = 1.4; magnification level 63X). To examine the signals arising from calcifications stained with Alizarin Red S relative to potential autofluorescence, confocal spectral imaging was used to verify the presence of Alizarin-derived signals with expected emission maxima at 650 nm. The detection window selected using the Leica acousto-optical beam splitter (AOBS) ranged from 645 to 665 nm for these measurements (633 nm HeNe Laser excitation). For reference, interference contrast images were collected using Leica tube optics HC 1X/B apparatus with a focusing Bertrand lens for setting the contrast.

Micro CT imaging technique. Formalin fixed human coronary segments (≈25 mm length, N = 24) obtained at autopsy were scanned using a General Electric Healthcare eXplore SP Pre-Clinical Specimen micro CT acquisition and analysis system. For image acquisition, 720 consecutive X-ray projections were taken, obtaining 7µm isotropic voxel resolution images. Mineral density was calibrated using a phantom containing hydroxyapatite, air, and water. Initial reconstructions of the whole volumes were carried out at 35µm voxel resolution. Due to computational limitations to handle digital data sets above 800 MB, the digital volumes were sectioned in consecutive volumes of interest (VOI) consisting of the whole vessel circumference and about 3 mm in height, which were then reconstructed at 7 microns resolution, resulting in 8-9 sections per sample. 3-D images were rendered and visualized using the Microview 3-D volume viewer software from GE. The presence of mineralized tissue particles was analyzed in each VOI.

2.3 Theoretical model for new hypothesis.

Most existing models of fibrous cap rupture (Richardson *et al*., 1989; Loree *et al*., 1992; Cheng *et al*., 1993; Huang *et al*., 2001; Finet *et al*., 2004; Tang *et al*., 2005) have been based on FEM calculations of calcified tissue cross-sections with a lipid core where the detailed geometry has been obtained from histology or IVUS imaging. A single element in such calculations would be larger than the cellular-level impurity in our hypothesis. In this paper we present an analytical solution for the stress concentration around a minute impurity in a thin tissue layer whose thickness is typically two to ten times the diameter of the impurity and whose location can be varied across the cap. The

purpose of the model is to test the quantitative feasibility of the new hypothesis and provide a framework for understanding the importance of the size of the impurity and its location.

Our three-dimensional theoretical model shown in Fig.2-1 consists of a rigid inclusion eccentrically located between the top (lumen) and bottom (lipid core) boundaries (Fig.2-1). The circumferential tensile stress in the fibrous cap is modeled by unidirectional tension T_0 applied at infinity; the top and the bottom boundaries are considered to be stress-free. Let the origin of coordinates be at the center of the inclusion with the z axis normal to the surfaces. The spherical and cylindrical coordinates are denoted by (r, φ, θ) and (ρ, φ, z) respectively. For convenience, r, z, ρ and all other lengths are made dimensionless by scaling relative to the half-thickness of the tissue layer. In such notation the upper (lumen) and lower (lipid core) surfaces of the fibrous cap are represented by $z = \pm 1 + c$, where c, the eccentric distance between the origin and the midline of the plate, is $< 1 - a$. To solve the problem we apply the Navier-Lame equations of linear elasticity for the case of equilibrium with no action-at-a-distance forces:

$$(\lambda + \mu)\, \Delta\, (\Delta\, \mathbf{u}) + \mu\, \Delta^2\, \mathbf{u} = 0, \qquad (1)$$

where u (u, v, w) is the displacement vector and λ and μ are the Lame constants, the stress-free boundary conditions at $z = \pm 1 + c$, the perfect bonding conditions at the rigid spherical inclusion – tissue interface at $r = a$, and the condition that the normal stress in the plate in the x direction tend to a uniform stress T_0 as x tends to $\pm \infty$. For detailed boundary conditions, see Appendix A.

Although the above boundary value problem is three-dimensional, it can be solved analytically without resort to numerical methods. The approach is patterned after the solution technique developed by Tsuchida *et al.* (1976) for the problem of an eccentric spherical cavity under uniaxial tension. In the latter problem the authors were interested in the stress concentration around a void space created by a spherical bubble. According to their approach, components of the displacement **u**(u,v,w) are first expressed in terms of six cylindrical harmonic functions φ_0, φ_1, φ_2, φ_3, φ_4, λ_4 which satisfy boundary conditions (2) and the normal stress condition (4) at infinity. These functions are defined in Appendix A. The cylindrical harmonics are then expressed in terms of spherical harmonics which are also required to satisfy the stress-free boundary conditions (2). The boundary conditions at the inclusion-tissue interface (3) lead to an infinite system of linear equations for the unknown coefficients of the spherical harmonics which are then truncated to provide the desired numerical convergence. After solving for the coefficients, one can calculate the stresses and deformations at any point within the tissue layer. A more detailed outline of the solution is given in Appendix A.

2.4 Results

2.4.1 Local stress concentration around minute spherical inclusions embedded in a fibrous cap. The quantitative feasibility of our new hypothesis was explored using the theoretical model in Fig. 2-1 to predict the factor of stress concentration (FSC) surrounding a spherical inclusion in the fibrous cap. Fig.2-2A shows the distribution of calculated radial stress concentration σ_r/T_0 at the matrix-inclusion interface when the dimensionless radius of the inclusion is $a = 0.1$ or $a = 0.5$, and the eccentric distance is c

= 0 or c = 0.4 and $\varphi = 0^o$. One observes from the figure that the presence of a perfectly rigid inclusion almost doubles the tension (adhesion stress) at the "poles" A, A' ($\theta = 90^o$, $\varphi = 0^o$ and $\varphi = 180^o$, Fig.2-1) in the direction of the applied tension T_0. In the classical theory of Goodier (1933) for a rigid spherical inclusion in an infinite medium the adhesion stress at the poles would exactly double. Surprisingly, the tensile stress intensification is scarcely affected by the relative size of the inclusion since the curves in Fig.2-2A corresponding to inclusion radii a = 0.1 and a = 0.5 are very close to one another and can be distinguished only at $\theta \approx 90^o$ and the curves for c = 0 and 0.4 are indistinguishable. The effect of a free surface on the stress concentration is demonstrated in Fig.2-2B for a = 0.1, 0.2, 0.3, 0.4, 0.5, 0.6. Maximum tensile stresses at A and A' tend to decline slightly as the inclusion approaches a free surface; the tendency is more noticeable for larger inclusions. One also notes that the larger inclusions are more stable and that the value of FSC decreases with increasing size. This behavior is similar to the much larger calcifications observed in IVUS where finite element calculations predict greater mechanical stability when calcified plaques are present (Huang *et al.* 2001). This strengthening occurs since the model does not allow for debonding and the calcification is more rigid than the surrounding material.

The theoretical model also allows us to estimate the peak circumferential stress (PCS) in the fibrous cap of atherosclerotic plaque arising from the presence of a calcified macrophage or SMC. Finet *et al.* (2004) have performed finite element calculations to predict the effect of cap thickness on the stability of fibrous cap atheroma based on typical *in vivo* IVUS images. The predictions of this model, which are given by line 1 in Fig. 2-3, show that PCS increases exponentially and will exceed the average maximum

circumferential stress in ruptured plaques of 545 kPa (Cheng *et al.* 1993) for plaque geometry 1 in Fig. 1 of their paper when the fibrous cap thickness is ≈25 µm. These predictions are based on the material properties used in Cheng *et al.* (11). The stresses indicated by line 1 are the PCS for a lumen pressure of 14.6 kPa (110 mm Hg) in the absence of a calcified macrophage. Lines 2 and 3 show how this PCS would increase if rigid inclusions of 10 and 20 µm diameter, respectively, approached to within 5 and 10 µm distances, in that order, from the lipid pool. Results of the calculations presented in Fig.2-3 provide a plausible explanation of the paradox that most plaque ruptures occur close to a region of high circumferential tensile stress, defined as a stress of more than 300kPa, but ruptures are not necessarily located at the points of maximum stress. According to Fig.2-3, a calcified macrophage located in an area of high circumferential stress (> 300kPa) can intensify this stress nearly two fold to ≈600 kPa when the cap thickness is < 65 µm.

2.4.2 Confocal microscopy evidence of microcalcifications in the fibrous cap. The results of our theoretical model were the catalyst for an intensive search for cellular-level solid inclusions within the cap proper. We have developed a confocal laser scanning microscopy technique using a Leica DM IRE2 microscope and Alizarin Red S stain to demonstrate the presence of microscopic calcific inclusions in atherosclerotic plaques from human arteries. As shown in Fig. 2-4, the Alizarin Red S staining technique provides high contrast in confocal images, with near negligible levels of background fluorescence. In this figure, panel A shows a necrotic core containing orange-red features from individual confocal optical sections obtained using Alizarin Red S – specific

detection. Panel B is obtained by overlaying the Alizarin confocal images with interference contrast images. The numerous cellular- and subcellular-level calcifications observed in the lipid core in Fig. 2-4A reveal two characteristic calcifications, spherical calcifications with dimensions comparable to an entire macrophage or SMC, and subcellular calcifications as small as 1-2 μm which are either of vesicular origin and extracellular, or intracellular calcified organelles. This image shows that Alizarin Red S is quite sensitive to very small deposits ≈10 μm. In some cases the Alizarin dye incompletely penetrated the calcification and an annular staining pattern was evidenced when the optical section sampled an intersecting plane (calcifications in center of Fig. 2-4A).

Figs. 2-4C and D represent the first experimental evidence for the existence of cellular-level calcifications in a fibrous cap. Fig. 2-4C shows two Alizarin Red S stained calcifications in close proximity, one the size of a single cell (≈10 μm) and the other, an elongated calcification that is several times the diameter of the single cell inclusion. Since we were unable to reconstruct a three-dimensional image for this histological section, it is not possible to determine the full inclusion shape; however, the confocal imaging technique allows us to perform a 3D reconstruction of the two calcifications within the section thickness (≈30μm). This partial reconstruction is shown in Fig. 2-4D.

2.4.3 Micro CT assessment of cellular-level calcifications in fibrous caps of atherosclerotic lesions. Micro CT images provide precise plaque visualization based on relative gray-scale attenuation differences within the lesions. Figure 2-5A shows a sagittal section of a 25 mm coronary segment, in which different tissue constituents

within the sample can be readily distinguished. In particular, air (black), soft tissue (light gray), mineral (white), and lipid (dark gray) are resolved. Initial analysis of coronary segment reconstructions with 35 μm resolution detected five advanced atheromatous lesions with fibrous caps and lipid cores. Further reconstructions of these soft plaques at 7 μm resolution revealed the presence of cellular-level calcifications in a thick cap of one of these lesions. Fig. 2-5B shows a cross section corresponding to the plane indicated by the arrow in Fig. 2-5A with three microcalcifications (circled) in a thick cap (≈250μm). Similar to the confocal images shown in Fig. 2-4, this micro CT image demonstrates that these cellular-level calcified inclusions in the cap are rare compared to the numerous calcifications seen at the bottom of the necrotic core (Fig. 2-5B, arrows). The cross section also shows 2 nearly spherical macrocalcifications, ≈300μm diameter at the plaque shoulders.

2.5 Discussion

Our hypothesis that minute cellular-level microcalcifications of typically 10 μm diameter in the fibrous cap can cause its rupture provides an important new insight into the mechanism of fibrous cap rupture and also resolves a long standing paradox as to why rupture does not always occur at the location of what was previously thought to be maximal tissue stress. The model predicts that minute spherical calcifications can increase the local stress around the embedded particle by nearly a factor of two at the poles of the tensile axis and that this amplification, quite surprisingly, is nearly independent of the size of the particle and relatively insensitive to its position in the fibrous cap. One of the striking results of the theoretical model is that it predicts that cap

rupture can occur in the center of a fibrous cap whose thicknesses is < 65 μm in close agreement with the empirical observations of Virmani *et al.* (2003).

Our hypothesis provides a plausible explanation for the paradoxical observation that approximately 40% of ruptures are observed in the center of the cap, and not at the plaque shoulders where finite element calculations predict the maximum values of circumferential stress (Cheng *et al.* 1993; Maehara *et al*. 2002). Using FEM analysis Cheng *et al.* (1993) calculated the stress distribution in specific coronary artery lesions that caused lethal myocardial infarction at a mean intraluminal pressure of 110 mm Hg and compared it to the stresses in control stable lesions. The average maximum circumferential stress in ruptured plaques without cellular-level solid inclusions was significantly higher 4091±1199 mm Hg (545± 160 kPa) than the average maximum stress found in stable specimens 1444±485 mm Hg (193±65 kPa), but not all plaque ruptures occurred at the region of the highest stress. In 7 of 12 ruptured lesions rupture coincided with the location of the maximum circumferential stress, while in 10 of 12 lethal lesions rupture occurred where calculated stress wasn't maximal but was more than 2250 mmHg (300kPa). The near doubling of the local stress due to the presence of minute calcifications in fibrous caps of these lesions can explain why rupture often occurs in secondary stress concentration regions. Our theoretical analysis predicts that the presence of a calcified cellular inclusion in the shoulder would be even more dangerous than in the central portion of the cap since the background stress here is greater and its doubling would make this region especially vulnerable. Thus, we propose that the site of cap rupture depends on the relative location of both the circumferential stress concentration and whether minute cellular-level microcalcification is present in the cap. Furthermore,

the average maximum stress of 545 kPa could be the rupture stress of the cap if no cellular-level solid inclusions are present.

The recent study by Tang *et al*. (2005) revealed another paradox in the assessment of plaque vulnerably. Their 3-D MRI-based computational model with multicomponent plaque structure and fluid-structure interaction (FSI) predicts that global maximal stress often appears at healthy parts of the vessel where vessel walls are thinner than the diseased plaque side or vessel curvature is large, though rupture does not occur at these sites. To resolve this paradox, the authors advance a "local maximal stress hypothesis" suggesting that local maximal stress values at critical locations may be more closely related to possible plaque rupture and should be used for more accurate mechanical plaque assessment. Preliminary results based on calculating the Stress-Based Computational Plaque Vulnerability Index (CPVI) showed a good correlation with plaque stability assessment given by histopathological analysis. This index is consistent with our hypothesis since a cellular-level calcification located at the critical site can nearly double their computed stress. Although these microcalcifications cannot currently be detected by standard imaging techniques, the present resolution of IVUS is ≈120 μm and OCT 15 μm, future development of the OCT technique might allow *in vivo* detection of these inclusions in thin fibrous caps. Such microcalcification assessment combined with advanced *in-vivo* image-based FEM/FSI models will provide more accurate quantitative assessment of plaque stability.

Our theoretical prediction that cellular-level calcifications can be responsible for plaque rupture might seem counterintuitive at first because much larger punctate calcifications (10^6 times the mass of a single cell) have been shown to be stabilizing by

FEM calculations (Huang *et al*. 2001; Imoto *et al*., 2005). Computational analysis applied to typical ruptured or stable human coronary atherosclerotic lesions reveals that mm size or larger calcifications deeper in the intima do not increase fibrous cap stress in the lesions (Huang *et al*. 2001). In contrast to a lipid pool, which dramatically increases cap stresses, bulk calcification doesn't seem to decrease the mechanical stability of the coronary atheroma. The most recent three-dimensional FEM calculations of the longitudinal stress distribution within atherosclerotic plaques based on a simplified axisymmetric geometry demonstrated that superficial mm size calcified plaques adjacent to the lipid core led to a decrease in the peak longitudinal stress value at the fibrous cap just above the lipid core (Imoto *et al*., 2005). Our model also predicts that the larger inclusions are more stable and the value of circumferential stress concentration decreases with increasing size. This behavior is similar to the much larger calcifications observed in IVUS where FEM calculations predict greater mechanical stability when calcified plaques are present (Huang *et al*. 2001). This strengthening occurs since the model does not allow for debonding and the calcification is more rigid than the surrounding material. Larger calcifications are also frequently observed beneath or at the edges of lipid pools, as seen in Fig. 2-5B, where the wall is thicker. For these larger calcifications the stress is also nearly doubled, but the background stress is much lower and even with a two fold increase in stress, the total stress would not exceed the threshold stress of 300 kPa.

The presence of small cellular- and subcellular-level calcified inclusions in necrotic cores of advanced atherosclerotic lesions has been reported in a number of histological studies (Stary 2001, 2003; Virmani *et al.* 2003). These microcalcifications have been mentioned in several intravascular imaging studies as a coronary calcification

pattern that is extremely difficult to detect. For instance, Friedrich *et al.* (1994) describe microcalcifications as small flecks of calcium with single fleck size $\leq$ 50 μm in their intravascular ultrasound study of intralesional calcium patterns. Only 17% of these microcalcification lesions were detected correctly by intracoronary ultrasound in contrast to 89% of all dense calcified plaques. Similarly, a frequency based spectral analysis of unprocessed ultrasound data (Moore *et al.* 1998) demonstrated that although microcalcifications reflect slightly more ultrasound energy than moderate fibrosis and less than dense fibrosis, the echoreflectivity of the plaque cannot be used alone to identify microcalcification from moderate fibrosis. These cellular-level calcifications in the necrotic core are not dangerous from a mechanical standpoint since they reside within a viscous lipid pool that does not support significant tensile stress. They are essentially floating debris without interface stresses. This is the exact opposite of a microcalcification that would occur in the fibrous cap as shown by our theoretical model.

Our new hypothesis for fibrous cap rupture is inspired by the classical theoretical studies of Goodier (1933) who examined the effect of minute solid spherical impurities in rubber tires as a cause of their failure. Failure will not occur unless there is debonding (failure at the tissue-particle interface). The most frequent cause of debonding is the formation of a minute cavitation bubble at the interface, which then rapidly expands. Experiments by Gent and Park (1984) showed that debonding occurred at the interface between the solid impurity and rubber because of the large mismatch in hardness of the materials and the local stress concentrations that develop at the poles of the impurity along the tensile axis as a result of this mismatch. Classical experiments with spherical impurities in elastomeric materials clearly demonstrate the creation of these cavitation

bubbles. The maximum circumferential stress of 4091 ± 1199 mm Hg (545 ± 160 kPa) estimated by Cheng *et al*. (1993) in ruptured plaques is almost equivalent to six atmospheres and, thus, far greater than needed to produce a negative pressure or vacuum at the failure interface. We emphasize that the present theoretical analysis doesn't incorporate debonding per se, but clearly demonstrates the possibility that this can occur. Future experimental studies are needed to demonstrate the possibility of such failure in coronary arteries with microcalcifications.

Another example of the influence of inclusions on the strength of materials is the reduction in fatigue strength of steels due to the stress concentration introduced by an inclusion. In high-hardness steel cracks often initiate preferentially from nonmetallic inclusions either on or beneath a free surface of a specimen, and lead to final fracture. Since the 1933 classical study of Goodier (1993), numerous theoretical or experimental investigations have been performed to obtain a better understanding of the stress fields due to inclusions in an elastic medium. However, most of the studies had been focused on inclusions within an infinite medium, and thus the results could not be applied to the analysis of fractures of high-hardness steels where a free surface has a strong influence on the stress field. Tsutsi and Saito (1973) were the first to analyze the problem of a semi-infinite body containing a perfectly bonded spherical inclusion under axisymmetric tension to see the effect of a free surface on the stress field. Their calculations showed that the effect of a free surface is significant when the inclusion is soft. On the other hand, if the inclusion is rigid, the maximum tensile stress appears to be insensitive to its position within the semi-infinite plate and tends to decline slightly as the inclusion approaches a free surface similar to our observations in Fig. 2-2B. Shortly after this

Nakahara and Tsuchida (1979) developed solutions for a symmetrically located spherical inclusion under uniaxial tension and showed large variation of the stress concentration as a function of its hardness. The 3D asymmetric problem, where a rigid spherical inclusion is arbitrarily located within a thin plate, is treated herein for the first time. A closed form truncated series solution for stresses and displacements is represented by a combination of a solution which is regular outside of the inclusion and a solution which is regular in an infinite plate. This solution is derived using an approach similar to that proposed by Tsuchida *et al.* (1976) for the problem of an eccentric spherical cavity under uniaxial tension.

The predictions of our theoretical model were the catalyst for an experimental search for probable weakening factors in the cap responsible for creating stress levels sufficient for its rupture. There were no prior reports, to our knowledge, of cellular-level solid inclusions in the cap proper. Our initial effort was to develop a confocal laser scanning microscopy technique that would clearly identify calcium. This was suggested by the fact that macrophages and SMCs in the necrotic core were observed to calcify after apoptosis. Therefore, it seemed plausible that both these cell types could undergo apoptosis and calcification in migrating across the fibrous cap of the lesion. Alizarin Red S had already been used to examine large calcifications in calcified heart valves (Bernacca *et al.* 1994). This method had been shown to be a useful addition to traditional histological methods available for the study of the calcification processes. In contrast to histological sectioning, confocal laser scanning microscopy doesn't require sample dehydration and processing and allows one to study biological materials in their normal hydrated state. Furthermore, measurement of fluorescent reporter group mobility and

localization within structures can provide important information regarding the biochemical, biophysical and structural status of calcifications and their context within the artery wall.

Having obtained the first confocal imaging evidence for the presence of cellular-level microcalcifications in the cap proper, we sought a 3D nondestructive imaging technique which would allow a systematic analysis of intact and unprocessed coronary artery segments**.** Recently, Langheinrich *et al*. (2004) demonstrated the feasibility of using micro CT for morphological and quantitative analysis of macroscopic atherosclerotic lesions. Micro CT imaging provides an accurate characterization of lesion morphology due to the difference in density between air, soft tissue, lipid and mineral. In contrast to histologic processing, which requires fixation, dehydration, and/or some degree of decalcification before paraffin embedding to allow sectioning, micro CT imaging can be performed in unprocessed coronary arteries. This prevents mechanical and physiochemical artifacts, such as shrinkage of the specimen, and retains true calcification morphology because there no decalcification is involved. Another problem with histological analysis is the difficulty of obtaining adjacent sections and avoiding distortion during the sectioning process. Histologic microscopy also does not provide 3D information and as a destructive technique, is limited to a small number of two-dimensional sections. With micro-CT, a complete digital data set of the whole vessel is available. Using tomographic reconstruction algorithms, 3D images of the vessel wall can be generated that allow total stereoscopic visualization of the 3D microarchitecture. Due to all these advantages combined with reliable and clear mineral detection, micro CT

imaging appears to be the best method to assess the presence of microcalcifications in the cap of fibroatheroma lesions *in vitro*.

Finally, it should be emphasized that the purpose of the present experimental study was simply to confirm our hypothesis that microcalcifications do indeed exist in fibrous caps and not just in the necrotic core. It is clear that a large scale statistical study is needed to quantify and compare the likelihood of cellular-level microcalcifications in the cap of ruptured and non-ruptured plaques and to further validate our proposed hypothesis for fibrous cap rupture. Our initial experimental data show that these calcifications are very rare compared to numerous cellular- and subcellular-level calcifications observed in the lipid core (Figs. 2-4, 2-5). If there were many such calcifications one might anticipate that there would be a high risk of cap rupture and thrombus formation even if not all ruptures lead to occluding thrombi (Kolodgie *et al.* 2001).

Chapter 3 Micro-CT based three-dimensional finite element analysis of the new paradigm for vulnerable plaque rupture

3.1. Introduction

The first confocal and micro-CT images of microcalcifications in fibrous caps described in Chapter 2 made us realize that we would need a much more sophisticated theoretical model in order to evaluate their effect on plaque stability. First, the images show that some microcalcifications are not spherical, but can take on elongated shapes and they can also have neighboring microcalcifications. Second, in any given calculation an accurate model is needed to determine the background stress in the cap. The majority of existing FEMs are based on 2D geometries of the lesion cross-sections obtained from histology, OCT, IVUS or MRI. Such a 2D computational approach wouldn't be sufficient to precisely define the PCS in lesions with complex geometries containing large mm-size macrocalcifications and cellular-size microcalcifications in the cap.

To overcome these limitations, I develop in this Chapter a 3D multi-level FEM based on high resolution micro-CT images. First, the micro-CT imaging data is used to generate realistic 3D geometries of the lesion using image processing and segmentation software MIMICS. Then, the obtained realistic geometries are combined with a multi-level submodeling technique in FE solver ABAQUS in order to include the analysis of all types of coronary calcification which appear blue in the image. Our model consists of a macro-scale global model representing the whole segment and two nested submodels, one at the level of the necrotic core and the other at the level of the microinclusions. The

macro-scale model of the whole plaque includes large millimeter size calcifications at the bottom of the lipid pool and at its shoulders. The lowest level micro-scale model, which represents a segment of the fibrous cap, has a FE mesh refined enough to treat the detailed stress distribution around one or more microcalcifications in the cap proper. Both submodels contain approximately 1.5 M tetrahedral elements.

One of the most important factors contributing to plaque rupture is believed to be the peak circumferential stress (PSC) in the fibrous cap (Cheng *et al*., 1993; Lee *et al*., 1993; Huang *et al*., 2001; Finet *et al*., 2004; Tang *et al*., 2004, 2005). Several of these computational analyses have demonstrated that thin fibrous caps and large lipid pools increase PCS in the cap dramatically. This observation agrees with pathological postmortem studies of ruptured plaques (Virmani *et al*., 2000; Kolodgie *et al*., 2001; Virmani *et al*., 2003; Cheruvu *et al*., 2007). The majority of existing FE models of atherosclerotic lesions are based on 2D geometries of the lesion cross-sections obtained from histology (Cheng *et al*., 1993; Loree *et al*., 1992; Huang *et al*., 2001; Finet *et al*., 2004). Although histology provides excellent resolution and clear definition of soft tissue components, it can't retain the true morphology of a lesion with coronary calcification because some degree of decalcification is usually required to allow sectioning. It is also difficult to avoid distortion in obtaining adjacent sections and, therefore, hard to reconstruct 3D images. Chau *et al.* (2004) used optical coherence tomography (OCT) as a basis for their 2D finite element analysis and showed that OCT can provide a more realistic geometry than histology by avoiding structural artifacts common to histological processing.

Structural analysis based on intravascular ultrasound imaging (IVUS) of human iliac vessel segments performed before *in vitro* balloon angioplasty has been used to predict the locations of plaque fracture that usually accompanies angioplasty (Lee *et al*., 1993). Ohayon *et. al.* (2001) performed 2D FE analysis based on IVUS images of atherosclerotic coronary arteries recorded before and after balloon angioplasty to predict *in-vivo* plaque rupture locations. Recently, a 3D MRI based computational model of human atherosclerotic plaque with multi-component plaque structure and fluid-structure interaction was developed by Tang *et al*. (2005). Although OCT, IVUS and MRI can provide 3D data for plaque structure, in all these imaging techniques large calcifications are not clearly delineated and calcifications < 50 - 100 microns are invisible. In order to circumvent these limitations and create a more accurate 3D geometry of a coronary lesion including cellular microcalcifications in the cap, I develop a high resolution micro-CT based computational technique. We showed in Chapter 2 that micro-CT imaging could be used for clear detection of cellular-level microscopic calcifications in the thin fibrous caps of vulnerable lesions. To our knowledge, the present study is the first attempt to use micro-CT imaging data sets to generate realistic plaque geometries and 3D finite element meshes for computational analysis of biomechanical plaque stability. Although the approach can't be applied to *in-vivo* analysis of plaque stability, the insights gained from the *in-vitro* method are intended as an invaluable tool for exploring the basic mechanisms of plaque rupture.

In Chapter 2 the quantitative feasibility of our hypothesis for vulnerable plaque rupture due to the presence of cellular-level microcalcifications in the fibrous cap was evaluated using a model of a perfectly bonded spherical inclusion arbitrarily positioned in

an elastic cap of uniform thickness under tension. In this Chapter, I develop a much more sophisticated multi-level FE model of these cellular-level microcalcifications in the cap proper and perform a 3D computational analysis using our detailed micro-CT reconstruction. This reconstruction includes the shape of the microcalcifications, their proximity to one another and their relationship to the cap thickness.

3.2. Methods

3.2.1. 3D Reconstruction of Plaque Geometry and Tissue Property assignment

The 3D micro-CT imaging data obtained from the coronary segment with microcalcifications in the fibrous cap described in Chapter 2 (Fig. 2-5) was transferred to an image processing and segmentation software Mimics (Materialize). 3D plaque geometry and FE surface meshes were created by Mimics and exported to a commercial finite element package, ABAQUS 6.7.3, to build a volumetric tetrahedral mesh corresponding to the segment. The mesh was sent back to Mimics for property assignment based on the gray scale level attenuation of the original image data. In previous computational studies of atherosclerotic plaque two major material models were used, the linear elastic model (Cheng *et al*., 1993; Lee *et al*., 1993; Finet *et al*., 2004) and the hyperelastic Mooney-Rivlin model (Huang *et al*., 2001; Tang *et al*., 2004, 2005; Chau *et al.*, 2004). In this Chapter, material mechanical properties were approximated by linearly elastic materials (Table 1 from (Cheng *et al*., 1993)). To take into account the complex structure of the plaque constituents, we used a transverse isotropic material model, which assumes that the deformable medium has the same properties in the

circumferential and axial direction. Lipid and calcifications were modeled as incompressible, isotropic materials with a Young's modulus of lipid equal to 1/100 of the circumferential Young's modulus of a normal artery and the Young's modulus of the calcification 10 times that of the non-calcified tissue (Cheng *et al*., 1993). The baseline model of the real coronary lesion was modified using morphological operations in Mimics in order to study the effect of cap thickness on the PCS in the lesion.

3.2.2. Finite Element Analysis

The computational analysis was carried out with a commercial finite element package, ABAQUS (version 6.7.3). The major difficulty for the 3D image based mesh generation was the resolution required to evaluate the stresses around microcalcifications of only 10 – 20 μ diameter. The size of the finite elements required needed to be much smaller than 1 micron. This would result in an unrealistically high number of elements to model the entire coronary segment. Thus, we used a submodeling technique available in ABAQUS to study in detail a small area of interest in a global model, in our case, a region of high stress around calcified inclusions in the cap. First, a global model for the entire coronary segment without microcalcifications in the cap was created based on low resolution (35 μm) micro-CT image reconstruction using a relatively coarse mesh. The static global stresses were calculated for a mean physiological blood pressure of 110 mmHg (14.6 kPa) applied to the luminal inner surface of the vessel. Then, we created two submodels corresponding to a 1.2 mm thick circular segment of the artery and a segment of the fibrous cap with microcalcifications in it. These hierarchical submodels based on

the high resolution (7 μm) micro-CT reconstructions had a much more refined mesh and were driven by the global solution.

3.3. Results

In order to investigate the impact of calcifications on biomechanical plaque stability I used micro-CT imaging data of a human coronary lesion with a lipid core, large mm-size calcifications in the vessel wall and microcalcifications in the fibrous cap described in Chapter 2. Fig.3-1 shows the sagittal section of the segment (A), cross section of the same segment corresponding to the plane indicated by the arrow in Fig.3-1A (B), and the 3D vessel geometry reconstructed with Mimics. I used the ABAQUS submodeling technique to focus on the fibrous cap with microcalcifications for detailed stress analysis. For each modeling level a mesh convergence study was performed in order to create a finite element mesh that balances accuracy and computing resources. We kept increasing the Mimics generated mesh density and reanalyzing the model until the difference between results from two consecutive meshes was negligible. The global model mesh corresponding to the whole vessel (Fig.3-1C) consisted of 2.5 million tetrahedral elements with the average length of edges ≈80μm. Calculated stresses and displacements were used to drive the first level submodel shown in green in Fig. 3-2A. The submodel represents a 1.2 mm thick segment of the whole vessel where the area of maximum circumferential stress was observed. The submodel's morphological structure is shown in Fig. 3-2A. The lipid core (red), fibrous cap and macrocalcifications (blue) at plaque shoulders are included in the submodel consisting of 1.5 million elements (average length of edges ≈30μm). At the first level of submodeling microcalcifications in

the fibrous cap were not considered due to the large size of the elements. Only the second level submodel (Fig.3-2B) which corresponds to a segment of the fibrous cap shown in green in Fig. 3-2A has a finite element mesh refined enough to include microcalcifications. The average edge of its 1.4 million elements was ≈0.3 μm (Fig. 3-2C).

First, we calculated the 3D stress distribution due to the mean physiological blood pressure of 110 mmHg in the entire segment (Fig. 3-3C). Analysis of the results revealed that the global maximum of circumferential stress was observed in the fibrous cap area where macrocalcifications at the plaque shoulders and microcalcifications in the cap are located (Fig.3-1B). Fig. 3-3A shows the stress distribution in the plaque cross section. The maximum circumferential stress is 72 kPa.

In order to analyze the effect of macrocalcifications at the plaque shoulders on the global stresses in the lesion, we created a model with two calcifications replaced by fibrotic tissue. All other morphological features and load conditions were the same. The results showed that the location of the maximum stress didn't change, but its magnitude increased to 84 kPa (Fig. 3-3B). The observed stress reduction in the cap due to plaque calcification supports the idea that large calcifications have a stabilizing effect on the plaque. The model without macrocalcifications at the plaque shoulders in Fig. 3-3B allowed us to analyze the impact of the macrocalcific inclusions on the local stresses in the vessel wall by providing the background stresses. Figs. 3-4A and C show the detailed stress concentration around the macrocalcifications in the two inserts in Fig. 3-3A. Figs. 3-4B and D show stress distribution in these two inserts in the absence of calcifications. Stress concentration can be observed around both macrocalcifications in the direction of

applied load at the poles of the inclusions (15 and 22 kPa in A and C comparing to 8 and 17 kPa in B and D). The calcification in A also shows stress reduction at the equator from 25 kPa to 7 kPa, while the calcification in C doesn't have the area of reduced stress, the stress is actually increased from 30 to 36 kPa. In summary, the presence of two macrocalcifications at the plaque shoulders doesn't change maximum local stress significantly, but rather causes stress redistribution.

We used the second level submodel to evaluate the stress concentration around microcalcifications in the fibrous cap proper. The results shown in Fig. 3-5 demonstrate that the PCS at the inclusions - cap interface reach 96.2, 54.9 and 37.8 kPa. Since the background circumferential stress in the cap without inclusions was 42.6 kPa, 28 kPa and 18 kPa, stress concentration coefficients for the three calcifications are 2.25, 1.96 and 2.1 which is very close to the coefficients predicted by our analytical model of a spherical inclusion described in Chapter 2 (Vengrenyuk *et al.*, 2006). Fig. 3-5A demonstrates that stress concentration around one of the inclusions located in a high stress area of 42.6 kPa reaches 96.2 kPa. This is higher than the global maximum stress of 72 kPa in the cap without microcalcifications shown in Fig. 3-3A. These results show that the inclusion of cellular-level microcalcifications resulted in a significant (33%) increase of the PCS in the thick-capped fibroatheroma. Another result of this analysis is that the location of the maximum stress has shifted from the lumen side of the cap to the interface between the inclusion and soft tissue.

The goal of our next numerical simulation was to investigate the effect of microcalcifications on the PCS as a function of cap thickness. We applied Mimics morphological operations to our baseline geometry of a thick-capped fibroatheroma to

simulate the cap thinning process. A series of 3D models with cap thickness decreasing from the original value of 300 µm to 40 µm were created using fibrous cap erosion and lipid core dilation. As a result of fibrous cap thinning lipid core volume increased from 1.44 mm^3 corresponding to the original lesion shown in Fig. 3-1 to 5.8 mm^3 for the 40 µm cap model. For each of these models the global peak circumferential stress in the fibrous cap and the maximum local stress around microcalcifications were calculated and plotted as a function of cap thickness in Fig. 3-6, lines 1 and 2 respectively. The graph shows that the presence of microcalcifications in fibrous cap results in an additional area of high circumferential stress in the cap. Both peak stresses increase exponentially as a result of reducing fibrous cap thickness. While our original thick-capped (300 µm) model predicted a global PCS of 72 kPa and a maximum local stress around calcifications of 96.2 kPa, the 40 µm thin-caped model predicted a PCS of 435 kPa and a maximum local stress around microcalcifications of 344 kPa. Although the global PCS in the thin-caped models (cap thickness < 80 µm) is higher than the local stress concentration around the microcalcifications, this local stress also reaches the rupture threshold of 300 kPa for cap thicknesses < 50 µm and, therefore, can increase the vulnerability of the lesion. In order to simulate the maximum destabilizing effect of microcalcifications, we also placed them in the area of the global PCS, and recalculated the maximum local stresses due to their presence. This result is plotted in Fig.3-6, line 3.

The present 3D FEM also allows us to estimate the effect of calcification shape on the stability of fibrous cap atheroma. Lines 2 and 3 in Fig. 3-7 show how the global PCS in the cap would increase if an elliptical calcific inclusion with aspect ratio $\lambda = b/a = 2$ and 4, respectively, was located in the region of PCS with major axis b along the tensile

axis. The stresses indicated by line 1 are the cap PCS with a spherical inclusion ($\lambda = 1$). Results of the calculations presented in Fig. 3-7 show significant increase in stress concentration with increase of the inclusion aspect ratio.

Finally, the effect of microcalcification proximity on biomechanical plaque stability was evaluated by using confocal images of Alizarin Red S - stained microcalcifications in a fibrous cap of a human coronary lesion shown in Figure 2-4, Chapter 2. Fig. 3-8A is the 3D confocal image reconstruction of these calcific inclusions, one the size of a single cell (10 μm) and the other an elongated calcification that is several times the diameter of the single-cell inclusion. We created an idealized 3D model of these inclusions based on the confocal image reconstruction and calculated the stress distribution around them when a uniform tension is applied in the direction of the long axis of the larger inclusion. Results of the calculations presented in Fig. 3-8B predict that the maximum stress between calcifications near the pole of the elongated inclusion can intensify the cap circumferential stress about 6 times. The high value of stress intensification can be explain by the fact that 1) the elongated inclusion's shape is close to an elliptical inclusion with a high aspect ratio, and 2) there is a superposition of local maximum stresses around inclusion poles due to their close proximity.

3.4. Discussion

In this Chapter, I have developed a new micro-CT based multi-scale FEM of atherosclerotic lesions and applied the technique to evaluate the impact of calcifications of different size, shape and location on biomechanical plaque stability under a static load with a mean arterial pressure of 110 mmHg. Computational analysis of a thick-capped

fibroatheroma predicted that the large calcifications at the plaque shoulders and microscopic calcific inclusions in the fibrous cap have an opposite effect on the lesion stability. While the shoulder calcifications have been shown to reduce the PCS in the cap by 16%, Fig. 3-3, the presence of the microcalcifications in the cap increased the PCS by 33%, Figs. 3-5. This modest increase occurred because the microcalcifications were not in a region where the background stress in the absence of microinclusions was a maximum. A much larger PCS would be obtained if the microinclusions were located in region where the background stress was close to a region of PCS without the inclusion as shown by curve 3 in Fig. 3-6.

It is known that the size of the lipid core and fibrous cap thickness have the most significant effect on the stress level within a plaque. Fibrous cap thinning may lead to increase of stresses and conversion of a stable plaque to a rupture prone or vulnerable lesion. We used Mimics morphological operations, namely, lipid pool dilation and fibrous cap erosion and created a series of fibroatheromas with cap thickness decreasing from 300 µm to 40 µm to model the "cap thinning" process. The results showed the presence of an additional area of high circumferential stress in the cap due to the local stress concentration around microcalcifications in all generated models for the microinclusions shown in Figs. 3-2B, C. Although this maximum local stress around inclusions was lower than the global PCS for < 80 µm thickness caps, see Fig. 3-6, its value for a cap thickness of 40 µm was 344 kPa, more than the rupture threshold of 300 kPa. However, the thickness of the fibrous cap and the size of the lipid core are not sufficient to predict cap stability. The results in Fig. 3-6 indicate that the most significant

impact on plaque stability occurs when microcalcifications are located in close proximity to a region of PCS.

To our knowledge, this study represents the first attempt to use high resolution micro-CT imaging for an *in-vitro* 3D FE analysis of an atherosclerotic lesion. Most existing FEMs of atherosclerotic lesions are based on 2D geometries of the lesion cross-section obtained from histology, OCT, IVUS or MRI (Richardson *et al*., 1989; Loree *et al*., 1992; Cheng *et al*., 1993; Huang *et al*., 2001; Finet *et al*., 2004; Tang *et al*., 2005). Currently, histology is considered to be the "gold standard" for determining plaque geometry and composition. Although it provides excellent resolution and clear definition of plaque morphology, histological processing and sectioning introduces artifacts, especially in plaques with calcifications present. In OCT, IVUS and MRI large calcifications are not clearly delineated and microcalcifications < 50-100 μm are invisible. We used high resolution (7 μm) micro-CT imaging data to generate realistic 3D geometries of a coronary lesion with several large mm size calcifications and microcalcifications (10 – 20 μm) in the fibrous cap and combine this with a multi-level submodeling technique in ABAQUS. Our simulations strongly suggest that this approach is the best approach to analyze the role of coronary calcium in plaque stability *in-vitro*. In addition, it can be also used for analyzing the potential impact of coronary calcification on the outcome of balloon angioplasty, stenting procedures, coronary artery bypass grafting and other surgical procedures.

The calculated stress concentration coefficient around macro- and microcalcifications in the lesion are very close to the values predicted by our analytical model of an idealized spherical inclusion in an elastic cap of uniform thickness under

tension described in Chapter 2. Both calcifications approximately doubled the background stress due to the fact that the inclusion shape is close to spherical and they are located far from each other. In addition, our results in Figs. 3-7 and 3-8 indicate that microcalcification shape can have a dramatic effect on plaque stability. The presence of an elliptical calcification with an aspect ratio $\lambda = 4$ in a fibrous cap can intensify the PCS in the cap by a factor of three beyond that for a spherical inclusion. The most significant, a 6 - fold increase in stress, was predicted in Fig. 3-8 for an elongated inclusion in close proximity to a spherical. The results suggest that microcalcification shape and positioning have a profound effect on plaque stability.

There is an extensive literature based on in vivo IVUS, OCT and MRI imaging that attempts to correlate calcified plaque burden with the prediction of future coronary events. This literature, which is inconclusive, is briefly summarized below since it pervades current thinking. It is very difficult to critically analyze this literature unless one is able to identify a mechanism for cap instability. The calculations in this Chapter and the hypothesis proposed by Vengrenyuk *et al.* (2006) propose such a mechanism. Unfortunately, the entire current literature, which is based on *in vivo* imaging, fails to capture the cellular level microcalcifications in the cap proper that are analyzed in the present paper and in Vengrenyuk *et al.* (2006). These cellular level inclusions fall below the visibility of these in *vivo* imaging techniques and their frequency has not yet been established. In addition, the term speckled or diffuse calcification used in the literature can also apply to calcified macrophages and smooth muscle cells that reside in the lipid pool and, as such, can be considered floating debris. These small calcifications have no

effect on plaque stability since they are imbedded in tissue with small or no tensile stresses (these tensile stresses vanish in the lipid pool).

With the foregoing caveats we briefly analyze some of the better known papers that try to correlate calcified plaque burden with plaque stability. In one series of studies of sudden coronary death cases, over 50% of nonruptured thin-cap fibroatheromas showed a lack of macrocalcification or only speckled calcification on post-mortem radiographs of coronary arteries (Burke *et al*., 2001). In contrast, 65% of ruptured lesions demonstrated speckled calcification, with the reminder showing fragmented or diffuse calcification. Furthermore, the mean calcification score was significantly higher in ruptured than in nonruptured vulnerable plaques. The authors concluded that these data demonstrate the lack of specificity of calcium patterns in unstable coronary plaques, but suggest that mildly to moderately calcified segments are the most likely to rupture. IVUS studies, on the other hand, have led to an opposing view of the importance of calcification. Rasheed *et al.* (1994) showed that unstable clinical symptoms are associated with quantitatively less calcium. Similarly, Beckman *et al.* (2001) observed that culprit lesions in patients with stable angina pectoris (SAP) were more extensively calcified than those in unstable angina pectoris patients (UAP) and that patients who have had an acute myocardial infarction (AMI) had the least calcified culprit lesions. Subsequently, Ehara *et al.* (2004) recognized that there was a significant difference in the pattern of coronary calcifications between patients with AMI, UAP, and SAP. They observed that small calcium deposits which subtended an arc of $<90^{o}$ (e.g. the macrocalcifications at the shoulders seen in Fig. 3-1) from the center of the vessel and were described as “spotty” calcification, were significantly more frequent in the culprit

lesions of AMI as opposed to SAP patients. The culprit lesions of AMI patients were mostly characterized by small macroscopic calcium deposits. These authors suggest that it is not the identification of calcium per se that is important, but rather the size, extent and location of the deposits. This conclusion is supported by an IVUS analysis by Fujii *et al.* (2005), who showed that ruptured plaques had quantitatively less calcium, especially superficial calcification, but a larger number of small calcium deposits, especially deep calcifications. In contrast to the clinical observations that coronary artery calcification is associated with worse prognosis histology based 2D finite Element Analysis in Huang *et al.* (2001) showed that large calcifications adjacent to the lipid core are actually stabilizing due to the fact that PCSs are reduced when these calcifications are present. Our present results also support the stabilizing role of mm-size macroscopic calcifications even when they occur in regions of large curvature, such as the cap shoulder.

In conclusion, the present model calculations predict that cellular level calcifications by themselves are not dangerous unless they lie in a region of high background stress. This high level of background stress only occurs in caps whose thickness is < approximately 80 μm. Whereas a spherical microcalcification will increase PCS by a factor of two this can be increased several fold by elongated microcalcifications of the type depicted in Fig. 3-8. Even if a microcalcification does appear in a thin cap, if it is spherical in shape there is a good chance that the maximum stress surrounding the inclusion may not exceed the rupture threshold of 300 kPa defined by Cheng et al. (1993). The most dangerous situation is when a microinclusion appears in close

proximity to a region where the PCS is already high. This stress will be substantially increased if the inclusion is elongated.

Chapter 4 Computational stress analysis of atherosclerotic plaques in ApoE knockout mice

4.1 Introduction

Over the last decade and a half, genetically engineered mice have been widely used to study the pathogenesis and potential treatment of atherosclerotic lesions, as well as genetic, hormonal and environmental influences on development of atherosclerosis (Breslow 1996; Daugherty 2002; Altenburg *et al.* 2007). The development of the apolipoprotein E knockout and LDL receptor-deficient mouse models in inbred mouse strains greatly accelerated the pace of our knowledge about molecules and cellular phenotypes that affect lesion growth (Zhang *et al*. 1992; Plump *et al*. 1992; Glass *et al*. 2001). The majority of these studies have focused on the development of the disease in the aorta which is the largest and the most accessible experimental vessel. For example, fat-fed ApoE deficient mice have been demonstrated to develop the entire spectrum of atherosclerotic lesions very similar to those in human through the arterial tree (Reddick *et al*. 1994; Nakashima *et al*. 1994). The aortic lesions appeared as foam cell lesions as early as 8 weeks, and after 15 weeks advanced lipid-rich lesions with fibrous caps overlying large necrotic cores were observed at this site. Though many of the features of plaque development and progression that occur in human plaques are similarly observed in murine plaques, these mouse models have long been regarded as poor models to study plaque rupture because the aortic sinus lesions seldom show any signs of fibrous cap disruption. Several recent studies reported potentially unstable atherosclerotic lesions

in older apoE-deficient mice in another anatomic site, the proximal part of the brachiocephalic artery (Rosenfeld *et al*. 2000; Johnson *et al*. 2001; Calara *et al*. 2001; Williams *et al*. 2002; Johnson *et al*. 2005). The presence of plaque rupture was demonstrated by visible defects in the fibrous caps with thrombi extending from the lumen to the core. In contrast to aortic lesions, the BCA lesions develop rapidly, especially in high-fat-fed mice, with advanced plaques present after as few as 5 weeks. Williams and colleagues (2002) compared morphological characteristics of ruptured and intact BCA lesions in a large number of ApoE knockout mice using histological analysis. 51 of the 98 mice analyzed were found to have an acutely ruptured atherosclerotic plaque in the brachiocephalic artery. The ruptured plaques showed some characteristics of vulnerable plaques in humans, namely, larger lipid cores (intact, 35.9 $\pm$ 3.0%; ruptured, 50.7 $\pm$ 2.2%), more buried caps within the lesion (intact, 1.06 $\pm$ 0.12; ruptured, 2.66 $\pm$ 0.16) and thinner fibrous caps (intact, 4.7 $\pm$ 0.6 μm; ruptured, 2.0 $\pm$ 0.3 μm). The mean ruptured cap thickness in the study, 2.0 $\pm$ 0.3 μm, was much less than the 23 $\pm$ 19 μm mean thickness of the caps in human ruptured coronary lesions (Burke *et al*. 1997; Virmani *et al*. 2000). In this Chapter I will show that this order of magnitude difference in rupture thickness can be quantitatively explained using the microcalcification hypothesis proposed in Vengrenyuk *et al*. (2006, 2008) if the shape of the microcalcification in the human lesions is taken into account. Our finite element analysis of both lesions shows quite remarkably that the peak stresses in the human lesion will be nearly identical to the peak stresses in the BCA lesions at rupture if the length of the cellular microcalcifications in the cap proper first identified in Vengrenyuk *et al*. (2006) is roughly twice their diameter.

The unusual stability of aortic lesions compared to the BCA lesions in ApoE knockout mice is an unexplained paradox in developing a mouse model of plaque rupture. It has been suggested that there may be special circumstances relatied to blood flow or the mechanical properties of the vessel wall that protect the aortic sinus from rupture (Jackson *et al*. 2007). One of these special conditions can be mean wall shear stress (WSS). A recent study by Greve *et al.* (2006) showed that mean WSS along the infrarenal aorta was significantly greater in mice and rats compared with humans (87.6, 70.5, and 4.8 dyn/cm^2). Although the study doesn't provide any data on mean WSS in mouse BCA, it would also in all likelihood be much higher than in humans and, therefore, not explain the difference in stability of the aorta and BCA lesions. Another possible explanation of the greater stability of mouse aortic lesions compared to BCA lesions is the level of biomechanical stresses within the lesions.

Chapter 3 describes numerous computational stress analyses conducted to predict plaque rupture in human vulnerable plaque. The majority of these biomechanical models for vulnerable plaque stability are based on the premise that there is a critical tissue stress or rupture threshold for the integrity of the cap. This rupture threshold has been estimated to have an average value of 545 kPa and a minimum value of 300 kPa (Cheng *et al.* 1993) depending on the local elastin and collagen composition of the tissue. The peak circumferential stress (PCS) in the cap is considered to be the most important measure of this stress and is often used as a predictor of plaque rupture location. To our knowledge, there have been no previous attempts to perform numerical stress analysis for murine atherosclerotic lesions to estimate biomechanical stresses within the lesions due to blood pressure.

In this Chapter, I apply FEA to evaluate peak circumferential stresses in mouse aortic and BCA lesions to test the hypothesis that these stresses are responsible for the greater stability of aortic lesions in mice. The remarkable feature of murine aortic lesions is that their fibrous caps are very thin, 10-20 micron, but they never appear to rupture despite the fact that the average systolic and diastolic pressures in these mice are 125 and 90 mmHg respectively, and thus not very different than humans. From Laplace's law for wall tension and geometric similarity, one might intuitively suspect the PCS to scale much like that for a human lesion and, therefore, such a thin cap should be highly unstable. Furthermore, the heart rate is 580 beats per minute, an order of magnitude greater than humans, suggesting that cap rupture due to cyclic fatigue loading would be much more likely in mice than humans. We shall show that the fundamental difference between human and murine lesions is that the former are thick enough to have cellular level 10-20 μm microcalcifications in the cap proper (Vengrenyuk *et al.* 2006, 2008) whereas the caps of both the aortic and BCA murine lesions are too thin to include cellular calcific inclusions.

These observations are a paradox of great importance in developing a murine model of plaque rupture. In order to uncover the potential protective mechanism preventing aortic lesions from rupture, we applied two-dimensional (2D) histology based FEA to estimate stresses in intact advanced aortic and BCA lesions from 42-56 week-old high fat fed ApoE KO mice. It is known that the size of the lipid core and fibrous cap thickness have the most significant effect on the stress level within a human atherosclerotic lesion (Finet *et al.* 2004; Tang *et al.* 2004; Tang *et al.* 2005; Ohayon *et al.* 2008; Vengrenyuk *et al.* 2008). Fibrous cap thinning due to enzymatic degradation may

lead to increase of stresses and conversion of a stable plaque to a rupture prone vulnerable lesion (Kolodgie *et al.* 2001). We create a series of idealized lesion geometries with cap thickness decreasing from 25 to 2 μm to investigate how PCS in the fibrous cap depends on the cap thickness. In addition, the "cap thinning simulation" allowed us to predict the stress level within an idealized BCA lesion with fibrous cap thickness of 2 μm, the mean cap thickness in ruptured lesions (Williams *et al.* 2002), and compare it to the stresses in unstable human caps. This comparison has led to the unexpected prediction that the PCS in murine BCA lesions at rupture is nearly identical to the stress along the tensile axis of an elongated microcalcification with aspect ratio 2 in human vulnerable lesions with a ≈ 50 μm thick fibrous cap. Since several computational studies predicted that plaque macrocalcification might stabilize human coronary lesions (Huang *et al.* 2004; Vengrenyuk *et al.* 2008), three older (58-60 week-old) apoE KO mice were also studied to evaluate the role of larger calcific deposits in the stability of murine lesions. These larger plaques appear to provide the same stabilizing role in murine lesions.

4.2 Methods

4.2.1 Mice

We studied six 42-56 week-old female and male apoE KO mice maintained on a high fat diet. They were housed in a specific pathogen-free environment at Mount Sinai School of Medicine and used in accordance with protocols approved by the Institutional Animal Care and Utilization Committee. Animals were sacrificed with CO_2, then exsanguinated by intracardial perfusion with 40ml of PBS/EDTA (2mM), followed by 150-200ml of freshly prepared 4% (para)formaldehyde in PBS. Perfusion was

implemented with a peristaltic pump set to a constant flow rate, and allowed to continue for at least 30 minutes for maximal preservation of the vessels' natural configuration. In addition, calcification in aortic arches and innominate arteries of three older (58-60 week) mice was analyzed using calcium specific stain Alizarin Red S (Vengrenyuk *et al.* 2006).

4.2.2 Histology

Aortic arches and brachiocephalic arteries were embedded in optimum cutting temperature compound (OCT). Frozen sections of 6 µm thickness were collected at 30-µm intervals and stained with hematoxylin and eosin, Van Gieson, oil red O or Alizarin Red S. One cross-section containing the largest lipid core was selected for each lesion identified with histology staining.

4.2.3 Structural Analysis

Five aortic and six brachiocephalic lesions were selected as described above. Quantitative analysis of plaque composition was performed by image analysis in ImageJ 1.4 (NIH). Cross-sectional geometries were traced to identify regions of fibrous plaque, normal vessel and lipid pool. Geometric and structural information from each tracing was exported to Finite Element software, ABAQUS, for biomechanical analysis of the lesions. The 2D histology based stress analysis was performed using an anisotropic material model (Cheng *et al.* 1993; Finet *et al.* 2004) assuming plain strain and a systolic pressure of 16.6 kPa (125 mmHg). The adventitia, media, and fibrotic tissue were assumed to have different linear elastic properties in the radial (r) and circumferential direction (θ). The Young's modulus (E_r, E_θ) and Poisson ratio ($\nu_{r\theta}$) values were 20 kPa,

200 kPa and 0.01 for the cellular fibrosis; 100 kPa, 200 kPa and 0.01 for the dense fibrosis; 10 kPa, 100 kPa and 0.01 for the media, and 80 kPa, 800 kPa and 0.01 for the adventitia (Finet *et al.* 2004). Lipid was modeled as an incompressible (ν =0.49) and very soft isotropic material with Young's modulus equal to 1 kPa, the Young's modulus of calcification was estimated to be 10000 kPa (Cheng *et al.* 1993).

4.3 Results

A 2D histology based FEA was utilized to compare stress distribution within five aortic and six BCA advanced atherosclerotic lesions as described in Methods. Morphological characteristics of the modeled plaques and calculated peak stresses in their fibrous caps are summarized in Table 4-I. The most striking result of our analysis was that the predicted peak stresses in all aortic lesions were significantly lower than maximum stresses in BCA plaques. Table 4-I shows that the PCS in fibrous caps of aortic lesions averaged 205.8 kPa, while cap stresses in BCAs demonstrated the average value of 568.8 kPa. The results of computational stress analysis for a representative aortic and BCA lesion shown in Fig. 4-1, left and right panels respectively, provide an explanation for the large difference in cap stresses. Fig. 4-1B shows idealized reconstructions of plaque geometry based on histological images (Fig.4-1A) with tracings corresponding to the lipid core area (LC), fibrotic tissue, media and adventitia. The asterisks correspond to the minimal thickness of the aortic and BCA fibrous caps, 12 and 9 microns, respectively. Plaque cross-sectional area was larger in the BCA lesion (102 mm^2) than in the aortic

plaque (66 mm^2), while fractional volume occupied by the lipid core was larger in the aortic plaque (59%) compared to BCA lesion (41%).

Our numerical analysis revealed a significant difference in stress distribution within the aortic and BCA lesion. The right panel of Figure 4-1C shows that the maximum circumferential stress of 795 kPa in the BCA lesion was located in the thinnest area of the fibrous cap marked by an asterisk in Fig. 4-1B, while aortic lesion stress reached its maximum of 553 kPa under the lipid core as shown in the right panel. The most surprising result of the model is that the PCS in the 12 micron thick fibrous cap of the aortic lesion reached only 160 kPa, far below the threshold for human plaque rupture of 300 kPa. A human lesion with this level of stress in the cap would have had a cap of about 100 - 120 micron thicknesses and been considered stable (Finet *et al.* 2004; Vengrenyuk *et al.* 2008). This non-intuitive result can be explained by the difference in geometry of the typical aortic and BCA lesion. The left panel in Fig. 4-1 shows that the aortic lesion, in contrast to the BCA lesion, protrudes into the lumen taking the shape of a blister. When the vessel is pressurized the tensile stresses are transferred to the outer layers of the wall, whereas the fibrous cap and the necrotic core are in a state of compression. This serves to reduce the tensile stress at the shoulders of the cap making the lesion more stable and, therefore, making the cap more resistant to rupture.

In order to analyze the maximum cap stress as a function of cap thickness and predict stresses in BCA-ruptured lesions with mean fibrous cap thickness 2.0 ± 0.3 μm (Williams *et al.* 2002), we created a series of idealized plaque geometries based on the baseline models shown in Fig.4-1A with cap thickness varying from 25 micron to 2 micron. Figure 4-2A shows six idealized geometries generated from the real aortic plaque

with cap thickness of 2, 4, 8, 16, 20, and 25 microns. The corresponding values for the lipid content varied from 50% for 25 μm cap to 74% for the thinnest cap of 2 μm. Five idealized lesion geometries based on the real brachiocephalic lesion with cap thickness of 2, 5, 14, 20, and 25 microns and lipid content varying from 34% to 42% are shown in Figure 4-2B. Peak cap circumferential stresses were calculated for the generated sets of aortic and BCA lesions and plotted as a function of cap thickness in Fig. 4-3, lines 1 and 2 respectively. As was the case for our previous results shown in Fig. 4-1, all generated aortic lesions showed peak stresses < than 300 kPa in the cap proper. In contrast, peak stresses in all BCA lesions were larger than the threshold for human plaque rupture and even exceeded 545 kPa for caps thinner than 17 microns. The graph also shows that PCS in murine BCA lesions increases exponentially as a result of reducing fibrous cap thickness (line 2) reaching levels of > 1000kPa for thin 2-5 micron caps, while maximum cap stress in aortic lesions increases slightly with decreasing cap thickness with maximum values for thin caps <300 kPa. Several computational studies showed that human vulnerable plaques are characterized by a similar exponential growth of peak cap stresses with decreasing cap thickness (Finet *et al.* 2004; Tang *et al.* 2004; Vengrenyuk *et al.* 2008). In order to compare the magnitudes of murine and human plaque stresses, we used Figures 3-6 and 3-7 from Chapter 3 to plot cap PCS in a human coronary lesion as a function of fibrous cap thickness in the same Figure 4-3. The baseline thick-caped human atheroma lesion analyzed in the previous Chapter had three spherical microcalcifications, ≈ 20 μm diameter, located in close vicinity to each other in the fibrous cap shown in Figure 3-1. Curve 3 in Figure 4-3 shows global PCS in the human cap without cellular level microcalcifications in the analysis. Curve 4 demonstrates how the maximum cap

stress is increased due to the presence of the microcalcifications located within the region of global PCS, and line 5 predicts the effect of an elongated microcalcification with aspect ratio $\lambda = b/a = 2$ on cap stress. The plot shows that line 2 representing cap PCS in murine BCA plaques is shifted up by 500-600 kPa with respect to the stresses in human lesion without microcalcifications in the cap (line 3). The predicted mouse BCA stresses also exceed significantly the human cap stresses around spherical microcalcifications (line 4). However, comparison of lines 2 and 5 indicates that the peak stress in the murine brachiocephalic cap at rupture (2 μm) is nearly identical to the peak stress in a 50 micron human cap with an elongated cellular microcalcification with aspect ratio two.

Several recent studies demonstrated the presence of calcification in old apoE KO mice. In order to evaluate the impact of calcium on murine lesions stability, we studied three 58-60 week-old females and males from apoE KO mice maintained on a high fat diet. We sectioned the entire aortic arches and BCA of these older mice, which were heavily laden with continuous lesions in the arch. Most sections of lesions contained no calcium. However, large calcifications were still rather frequent and were encountered approximately every 400-μm along the arch. In none of the approximately 200 sections have we been able to detect microcalcifications embedded into the fibrous caps similar to human coronary lesions described in Chapters 2 (Figures 2-4, 2-5). Figure 4-4A illustrates an Alizarin red staining of aortic arch section from a 60-week old apoE KO female mouse. The section shows large calcifications on the shoulders of the plaques, features consistent with human lesions. In addition, a small 10-12 μm microcalcification (arrow, Fig. 4-4A) is located on the margin of a fibrous cap just overlying the lipid pool of a necrotic core. The calculations (Fig. 4-4B) showed that circumferential stress within

the lesion reached its maximum (red areas in Fig. 4-4B) in several regions: at the plaque shoulders, under the lipid core and below the left calcification. Similar to the previous results summarized in Table 4-I, the magnitude of the peak cap stress, 248.8 kPa, was below the threshold for human plaque rupture of 300 kPa.

The purpose of the next numerical simulation was to validate our hypothesis that macrocalcifications at the plaque shoulders have a stabilizing effect. We replaced the two large shoulder calcifications by fibrotic tissue and recalculated stresses under the same loading and boundary conditions. Maximum circumferential stress for the section without calcium was 267.5 kPa, 8% more than in the original model. The result obtained suggests that macrocalcifications in murine plaques as observed in human lesions by Huang et al. (2001) and shown in Chapter 3, Fig. 3-3 are reinforcing and increase stability.

4.4 Discussion

The first finite element solutions for the tissue stress distribution have been obtained for the murine animal model of atherosclerosis using histology images of high fat diet-induced lesions. These model predictions are of particular significance since they provide important insight into a fundamental paradox: why do the thin fibrous caps of human lesions rupture, whereas the much thinner caps of ApoE KO mice seldom rupture in aortic lesions although these caps can be as thin as 10 μm and are subject to similar lumen pressures. One would intuitively think that the tensile stress should easily exceed 300 kPa for such a thin cap and it would be highly prone to rupture. The results obtained have led to a most surprising prediction, namely that the PCS in the murine aortic lesion can be significantly less than humans although its cap thickness can be as little as 10 μm.

Our calculations showed that the average stress in aortic lesions was only 205.8 kPa, below the threshold for human plaque rupture of 300 kPa. A human lesion with this level of stress in the cap would have had a cap of approximately 100-120 micron thickness and have been considered stable (line 3 in Fig.4-3). In other words, the model showed that an aortic mouse lesion with a very thin, 10-20 micron fibrous cap is characterized by the same level of circumferential stresses as a thick-cap human fibroatheroma which seldom ruptures. The “cap thinning” numerical simulation shown in Figure 4-3 further supports our hypothesis that biomechanical stresses can be responsible for the unusual stability of aortic lesions in mice. Thin BCA caps (2-5 micron) in this simulation demonstrated high stresses of 1000 - 1400 kPa, while maximum tensile stresses in thin aortic caps of this thickness were 3 - 4 times lower, hardly reaching 300 kPa.

The non-intuitive result for murine lesions arises from the observation that there is a distinctly different behavior for aortic and BCA lesions. The former deform in such a way as to reduce peak circumferential stress in the cap, whereas the latter deform like human lesions in a manner that increases PCS. This prediction could explain why ruptures are seldom seen in high fat-diet induced aortic mouse lesions, whereas there appear to be at least occasional ruptures in BCA lesions (Rosenfeld *et al.* 2000; Johnson *et al.* 2002). This is due to a negative remodeling that occurs when the lesions take the shape of blisters that protrude into the lumen. All of the aortic lesions that we have observed in the six mice in this study have had this geometry. In marked contrast, BCA lesions appear to have a flat geometry that is closer to that observed in human lesions. One can think of this as a positive remodeling that leads to instability.

The process of coronary artery enlargement in response to plaque growth which maintains the lumen area was first described by Glagov and colleagues (1987). Their histopathology study discovered that due to the compensatory enlargement of human atherosclerotic lesions lumen stenosis may be delayed until the lesion occupies 40 percent of the internal elastic lamina. Despite the fact that positive remodeling avoids vessel stenosis, it can have dangerous consequences since it promotes plaque vulnerability. An *in vivo* study with intravascular ultrasound established a relationship between positive remodeling and plaque stability (Schoenhagen *et al.* 2000). In this study, positive remodeling was more frequent in unstable than in stable lesions, while negative remodeling, or vessel shrinkage, was more common in patients with stable clinical presentation. One of the explanations for the observed in *vivo* increase in plaque vulnerability at the sites of outward vessel wall remodeling is that coronary artery plaques have been shown to have higher lipid content and macrophage count, both markers of plaque vulnerability (Varnava *et al.* 2000). The importance of considering arterial remodeling index in addition to fibrous cap thickness for evaluating biomechanical plaque vulnerability was demonstrated by a recent FEA of cap stresses as a function of remodeling index (Ohayon *et al.* 2008). Our computational predictions for stress distribution within an aortic lesion shown in Fig. 4-1C, left panel, can explain the higher stability of negatively remodeled lesions. The color map of lesion stresses shows that some parts of the cap may be even compressed in a lesion protruding inside the lumen.

The difference in size between human and mice arteries requires development of different quantitative criteria for vulnerable plaque rupture. For example, a thin-cap

fibroatheroma with cap thickness < 65 micron and large lipid core has been defined as a more specific precursor of plaque rupture in humans (Burke *et al.* 1997). Even though all fibrous caps in mice are thinner than this, it would be unreasonable to conclude on this basis that all mouse plaques can be considered as vulnerable thin-capped lesions (Jackson *et al.* 2007). Our histology based FEA allows one to compare biomechanical stresses in human and mouse vulnerable lesions. The results shown in Figure 4-3 predict that murine ruptured lesions with mean cap thickness of 2 microns have stresses about 1400 kPa, four times higher than human ruptured plaques with a mean cap thickness of 23 μm without calcifications in the cap proper, but nearly identical to the local stress around an elongated microcalcification with aspect ratio two perfectly embedded in a 50 μm thick human cap. In addition, our "cap thinning" simulations further supported the previous observations that BCA lesions more closely mimic stress level and distribution in human vulnerable lesions. They demonstrated an exponential growth of peak cap stresses with decreasing the cap thickness predicted for human plaques by several computational studies (Finet *et al.* 2004; Tang *et al.* 2004; Vengrenyuk *et al.* 2008). In contrast to stresses within BCA lesions, aortic plaque stresses are shown in Figure 4-3 to only slightly depend on cap thickness.

The question that still needs to be resolved for the murine BCA lesions is why there aren't more frequent ruptures despite such high stresses in their fibrous caps. One possible explanation is that the WSS in mice is an order of magnitude greater than in human arteries (Greve *et al*. 2006). This elevated WSS may lead to compensatory changes in the density of the extracellular matrix and collagen content within mouse plaques that render them consequently more resistant to rupture (Jin *et al.* 2003). Another

reason for the greater stability of murine lesions can be related to plaque calcification. Several recent computational studies of calcified human lesions demonstrated that coronary calcifications have a significant effect on plaque stability depending on their size, shape and localization. While large millimeter size calcifications frequently observed adjacent to or under the lipid core have been shown to have a stabilizing effect (Huang *et al.* 2004; Tang *et al.* 2004; Vengrenyuk *et al.* 2008), we showed in Chapters 2 and 3 that cellular level microcalcifications, 10 - 20 μm diameter, in the fibrous cap proper can increase plaque vulnerability dramatically by creating stress concentration around these rigid inclusions (Vengrenyuk *et al*. 2006, 2008). Lines 3 and 4 in Figure 4-3 show that the presence of spherical microcalcifications embedded in the fibrous cap of a human plaque can almost double cap PCS due to the mismatch of mechanical properties at the inclusion/tissue interface.

Despite the fact that calcification in human lesions is a well-known occurrence, the tendency of plaques in apoE-deficient mice to calcify has only recently been studied. Aging apoE-deficient mice show progressively increased degrees of medial and intimal calcification in the aorta and BCA (Bennett *et al.* 2006), with a marked elevation in total extractable calcium particularly in females aged for 60 weeks (Rattazzi *et al.* 2005). Our computational results shown in Fig. 4-4 predicted that macrocalcifications in murine lesions, as observed for humans, are reinforcing and increase stability. At the same time we haven't been able to identify microcalcifications in the fibrous caps of any of the lesions in this study, probably, because, unlike a human lesion, the murine cap is too thin to contain a 10-20 μm cellular level microcalcification. All the above factors combined

can make the ApoE KO BCA lesion highly resistant to rupture despite their very thin caps and high level biomechanical stresses.

In conclusion, our computational model predicts biomechanical stress patterns in mouse BCA that are close to human vulnerable plaques, while murine aortic lesions showed stress behavior similar to stable lesions. Our FEA predicts similar stress levels in ruptured BCA plaques and thin-cap human atheromas with an elongated microcalcification in the cap proper. The results suggest that the proximal BCA artery of the fat-fed apoE knockout mouse is a better site to study pathophysiology of plaque rupture although they are too thin to contain cellular microcalcifications in the cap proper. Despite the absence of these microcalcifications the murine BCA lesions have stress levels that are quite similar to the PCS of the much thicker vulnerable caps of humans with such microcalcifications as shown in Chapter 2, Figs. 2-4, 2-5.

Chapter 5 Conclusion

Most acute coronary events and sudden coronary deaths have been associated with rupture of a thin fibrous cap overlying the necrotic core of thin-capped fibroatheroma lesions followed by thrombosis (Burke *et al*., 1997, 1999; Virmani *et al*., 2000). Despite major advances in treatment of coronary heart disease patients, a large number of victims of the disease who are apparently healthy die suddenly without prior symptoms. Available screening and diagnostic techniques are insufficient to identify the victims before the event occurs (Naghavi *et al.* 2003). The mechanism as to why some thin caps rupture and others do not is very likely the most important unanswered question in life threatening atherothrombotic lesions. This dissertation develop a new paradigm of TCFA rupture, suggesting that minute calcifications located in the cap itself increase the tissue stress concentration and vulnerability of the plaque. We propose that these microcalcifications can lead to cavitation induced debonding, a process in which the tissue in the cap will pull away from the calcified inclusion and tear when the tensile stress in the tissue due to blood pressure becomes too large.

In **Chapter 2** I used a 3D model of a perfectly bonded spherical solid inclusion arbitrarily positioned in an elastic cap of uniform thickness under tension to evaluate the quantitative feasibility of this new hypothesis. First, I derived a local analytical solution of the 3D boundary value problem using linear elasticity. This solution predicted a nearly twofold increase in the local peak tensile stress around the embedded particle at the poles of the tensile axis. Then, I combined this local analytical solution for the stress concentration around the inclusion with the histology based 2D finite element solution for

circumferential stresses in a fibrous cap previously obtained by Finet *et al*. (2004). The results showed that inclusions located in an area of high circumferential stress (>300 kPa) in the cap can intensify this stress to nearly 600 kPa, higher than the average rupture threshold, 545 kPa, when the cap thickness is ≈ 65 μm, in close agreement with pathology observations (Burke *et al.* 1997). The model also provided a plausible explanation for the paradoxical observation that 40% of ruptures occurred in the center of the cap where FE calculations didn't predict maximum stresses (Cheng et al. 1993; Maehara *et al*., 2002).

Having demonstrated the quantitative feasibility on the new hypothesis, first, I developed a confocal laser scanning microscopy technique using calcium specific stain Alizarin Red S to demonstrate the presence of microscopic calcific inclusions in fibrous caps of atherosclerotic plaques from human arteries. Fig. 2-4 provides the first experimental evidence for the existence of cellular-level calcifications in the fibrous cap proper. It shows two Alizarin Red S stained calcifications in close proximity, one a near spherical inclusion the size of a single cell (≈10 μm) and the other, an elongated calcification that is several times the diameter of the single cell inclusion. Second, I developed a 3D nondestructive micro-CT imaging technique to be able to analyze systematically a large number of intact and unprocessed coronary artery segments**.** The approach was used to identify three microcalcifications (≈10 - 20 μm diameter) in a thick fibrous cap of one out of 5 analyzed advanced atherosclerotic lesions (Fig.2-5). Similar to the confocal images shown in Fig. 2-4, the micro-CT images demonstrated that these cellular-level calcified inclusions in the cap are rare compared to the numerous calcifications seen at the bottom of the necrotic core. The micro-CT cross section also

shows 2 nearly spherical macrocalcifications, ≈300 μm diameter at the plaque shoulders. As we show in the next Chapter, these two macrocalcifications at the shoulders, whose volume is > 10^4 larger than the three circled microinclusions, are in fact stabilizing whereas the cellular calcifications in the cap proper, which lead to a doubling of the tensile stress at the poles of the micro-inclusions, are destabilizing.

In **Chapter 3** I developed a more sophisticated multi-level FE model of cellular-level microcalcifications in the cap proper and performed a 3D computational analysis using the detailed micro-CT reconstruction to evaluate the impact of calcifications of different size, shape and location on biomechanical plaque stability under a static load with a mean arterial pressure of 110 mmHg. Computational analysis of a thick-capped fibroatheroma described in Chapter 2 predicted that the large calcifications at the plaque shoulders and microscopic calcific inclusions in the fibrous cap have an opposite effect on the lesion stability. While the shoulder calcifications have been shown to reduce the PCS in the cap by 16%, the presence of the microcalcifications in the cap increased the PCS by 33%. A much larger PCS would be obtained if the microinclusions were located in the region where the background stress was close to the PCS without the inclusions. The results suggest that cellular-level calcifications by themselves are not dangerous unless they lie in a region of high background stress. The model predictions led to more refined hypotheses for fibrous cap rupture suggesting that the most dangerous situations occur when 1) a microinclusion appears in close proximity to a region where the PCS is already high, 2) the microcalcification has an elongated shape, or 3) there are two microcalcifications in close proximity to one another.

In **Chapter 4** I obtained the first finite element solutions for the tissue stress distribution for the murine animal model of atherosclerosis using histology images of high fat diet-induced lesions. These solutions provided an important insight into a fundamental paradox: why do the thin fibrous caps of human lesions rupture, whereas the much thinner caps of ApoE KO mice seldom rupture in aortic lesions although these caps can be as thin as 10 μm and are subject to similar lumen pressures. The model predicted that an aortic mouse lesion with a very thin, 10-20 μm fibrous cap is characterized by the same level of circumferential stresses as a thick-cap (100-150 μm) human fibroatheroma which seldom ruptures. In addition, the histology based FEA allowed to compare biomechanical stresses in human and mouse vulnerable lesions. The results predicted that murine ruptured lesions with mean cap thickness of 2 microns have stresses about 1400 kPa, four times higher than human ruptured plaques with a mean cap thickness of 23 μm without calcifications in the cap proper, but nearly identical to the local stress around an elongated microcalcification with aspect ratio two perfectly embedded in a 50 μm thick human cap. The results suggest that the proximal BCA artery of the fat-fed apoE knockout mouse is a better site to study pathophysiology of plaque rupture although they are too thin to contain cellular microcalcifications in the cap proper. The model predicted that these lesions have stress levels that are quite similar to the PCS of the much thicker vulnerable caps of humans with such microcalcifications.

In summary, I have advanced a new paradigm for vulnerable plaque rupture due to the local stress concentration around cellular-level microcalcifications in the cap proper. I used confocal and micro-CT imaging to demonstrate that these microscopic calcific inclusions do exist in the fibroatheroma caps, and 3D micro-CT based FEA to

show that these microcalcifications can critically increase PCS in the cap, augmenting its risk of rupture. These studies have the potential for explaining why some atherosclerotic lesions are more prone to rupture than others and, as a result, may improve the detection and treatment of vulnerable plaque.

Future directions

Although we have obtained very convincing experimental and theoretical evidence for the potential destabilizing role of cap microcalcifications, further studies will be required to test and confirm the proposed hypothesis. If I were to continue this research, I would be most interested in a large scale statistical study of a much wider sample of ruptured and non-ruptured lesions from patients who died of acute coronary syndrome (ACS). I would determine the frequency, size, shape, and spatial distribution of microcalcifications within the fibrous caps using high resolution micro-CT imaging as described in Chapter 2. The new multi-level 3D micro-CT based FEM developed in Chapter 3 can be used to evaluate the effect of microscopic calcified deposits on the stress distribution in TCFAs using accurate 3D geometries obtained from the high resolution micro-CT imaging. The developed computational approach can be further improved by incorporating calcium debonding into the FE analysis in order to model cavity formation, propagation and rupture. ABAQUS FE software has the suitable tool for this kind of analysis, the Cohesive Finite Elements.

It would be also very interesting to actually observe the hypothesized debonding at the calcification – tissue interface *in vitro* subjecting coronary artery tissue to uniaxial or biaxial tension. While performing this experiment on a fibrous cap containing

microcalcifications can be challenging due to the small size of the tissue specimen, it might be easier to demonstrate debonding around macroscopic calcifications embedded in the vessel wall similar to shoulder calcifications shown in Fig. 2-5. Another more realistic but difficult approach to inducing calcification debonding in the cap would be pressurizing the whole coronary segment and rupturing the cap.

Finally, I think that collaboration with an OCT imaging group could bring this project to a new level. The latest clinical study of plaque morphology in patients with ACS used OCT imaging with resolution of 10 – 20 micron (Tanaka *et al.* 2008). Although even this resolution wouldn't be sufficient to clearly visualize an isolated calcification in a thin fibrous cap, development of a signal processing algorithm might provide a tool to differentiate between caps with and without microcalcifications.

If these future studies of cellular-level microcalcifications in fibrous caps of human fibroatheroma lesions confirm the proposed hypothesis, a whole new approach for the identification of vulnerable plaque stability will have been discovered, aimed at the study, identification, genesis and prevention of microcalcification formation in fibrous caps in vivo.

TABLES

Table 4-I Plaque characteristics and cap stresses in aortic and BCA murine lesions.

Lesion #	BCA lesions				Aortic lesions			
	Cap thickness, μm	Lipid content, %	Plaque cross-sectional area, mm^2	Max cap stress kPa	Cap thickness, μm	Lipid content, %	Plaque cross-sectional area, mm^2	Max cap stress, kPa
1	10	41	102	795	12	59	66	160
2	9	36	173	440	17	33	181	267
3	15	36	69	338	8	48	88	128
4	5	33	189	510	15	46	84	226
5	12	41	178	490	10	51	95	248
6	6	43	88	840				
Mean	**9.5**	**38.3**	**133.2**	**568.8**	**12.4**	**47.4**	**102.8**	**205.8**

FIGURES

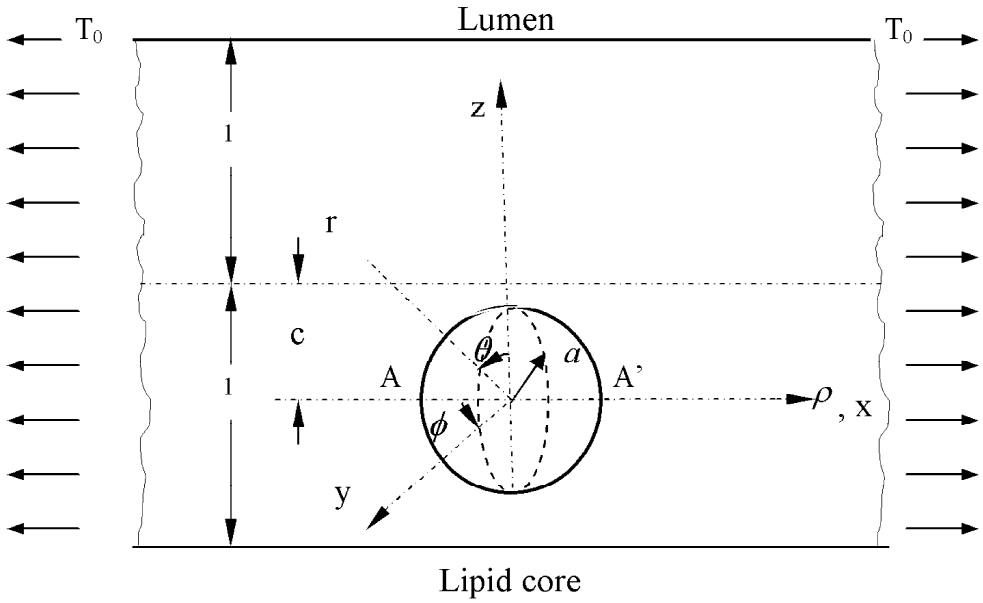

Figure 2-1. Mathematical model: geometry and coordinate system. A perfectly bonded rigid spherical inclusion with radius a in a fibrous cap.

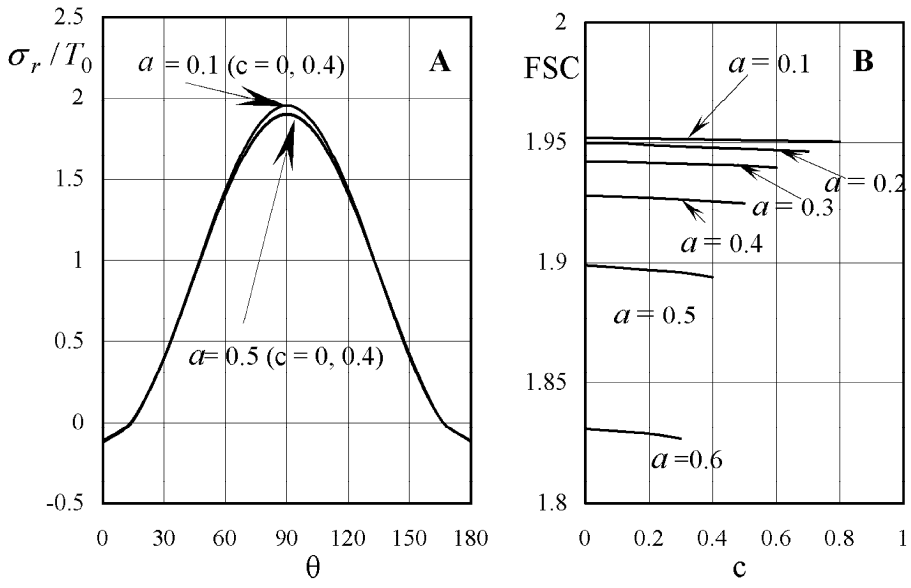

Figure 2-2. Stress concentration in a fibrous cap due to the presence of a rigid spherical inclusion. (A) Distribution of radial stress concentration σ_r / T_0 at the matrix- inclusion interface for the cases of a = 0.1, a = 0.5 and c = 0, 0.4 (ϕ = 0^o); (B) Effect of a free surface on factor of stress concentration (FSC) for a = 0.1, 0.2, 0.3, 0.4, 0.5, 0.6.

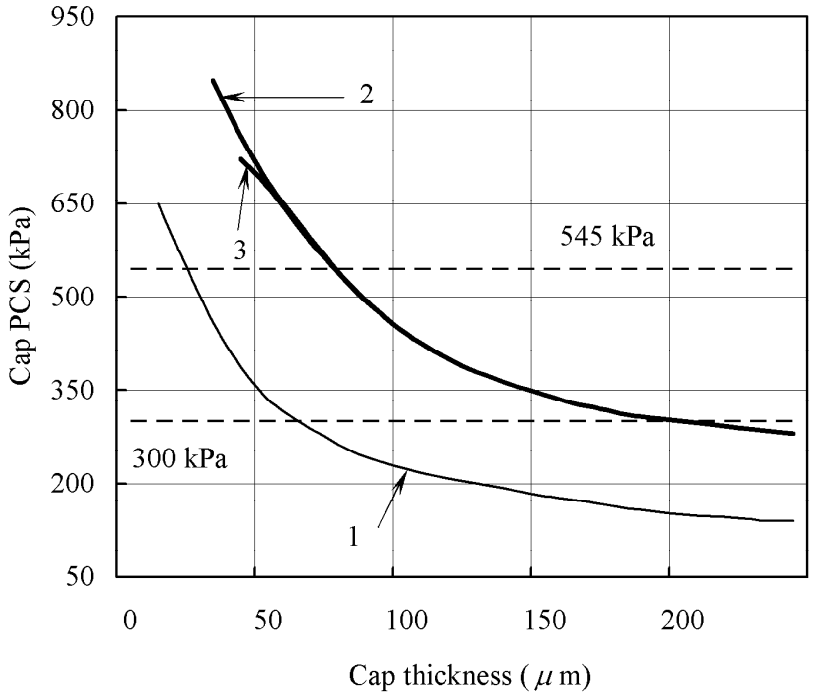

Figure 2-3. Changes in cap peak circumferential stress (PSC) with cap thickness for the case when cap tissue is homogeneous (line 1) and when it contains a rigid inclusion of 10 and 20 microns in diameter (lines 2 and 3 respectively).

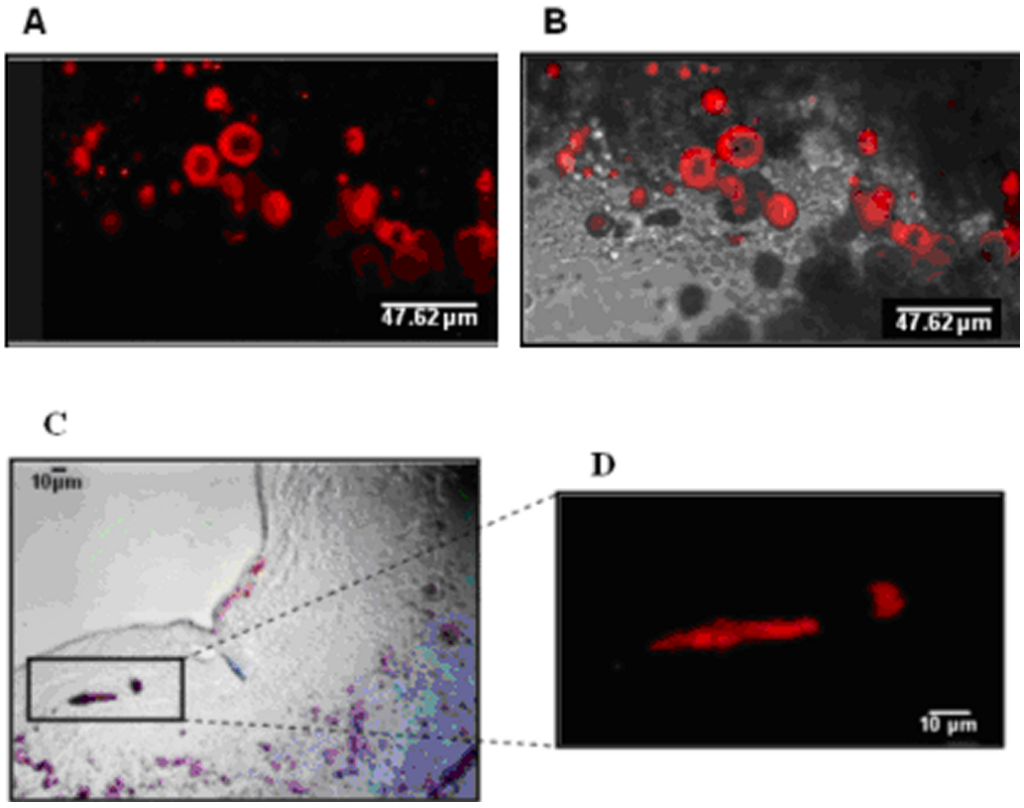

Figure 2-4. Confocal microscopy images of calcific deposits stained with Alizarin Red S in coronary artery lesions: numerous cellular- (≈10 µm) and subcellular-level calcifications in the necrotic core (A); overlay of image (A) with a transmission image (B). Calcified inclusions in the fibrous cap appear red in a section stained with Alizarin Red S (C); a 3-D confocal imaging reconstruction of section (C) within the slide thickness (D).

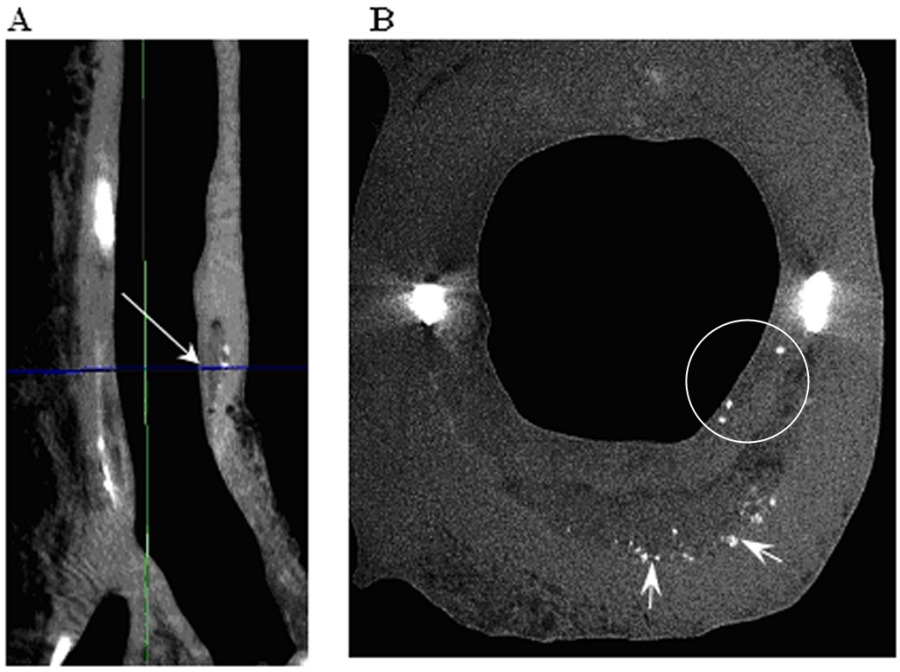

Figure 2-5. Micro-CT detection of cellular level microcalcifications in a fibrous cap: a sagittal view of a coronary artery segment with microcalcifications in the thick cap (35 µm resolution) (A); a cross section of the lesion (arrow in A) corresponding to the plane marked by an arrow in A with cellular-level microcalcifications ≈10 - 20 µm diameter in the cap (circled) and numerous calcific deposits at the bottom of the lipid pool shown by arrows (7µm resolution) (B).

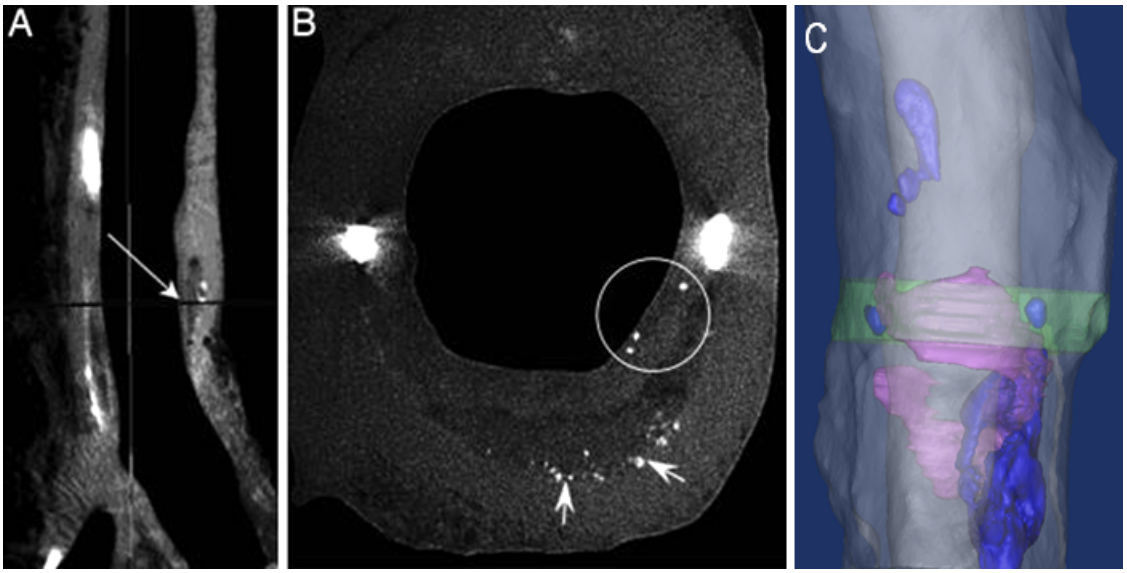

Figure 3-1. Micro-CT images (A, B) and reconstructed 3D geometry (C) of a coronary plaque with bulk calcifications (white in A and B, blue in C) and lipid core (dark areas in A and B, red in C). A small segment of the global model (green) containing fibrous cap with microcalcifications represents the first level submodel shown in detail in Fig.3-2A.

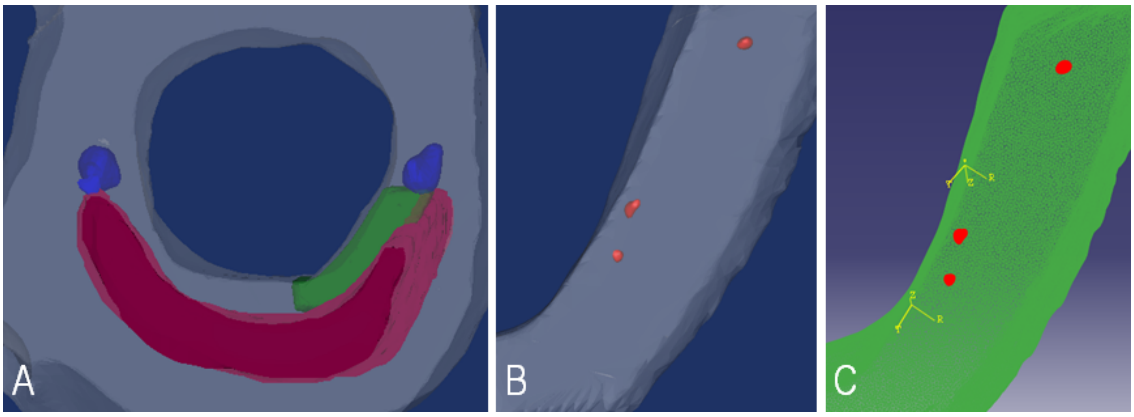

Figure 3-2. The hierarchy of Mimics/ABAQUS submodels. The first level submodel with macrocalcifications at the plaque shoulders (blue), lipid pool (red) and fibrous cap doesn't include microcalcifications in the cap (A). The submodel's cap fragment shown in green represents the second level submodel (B,C) which contains three microcalcifications.

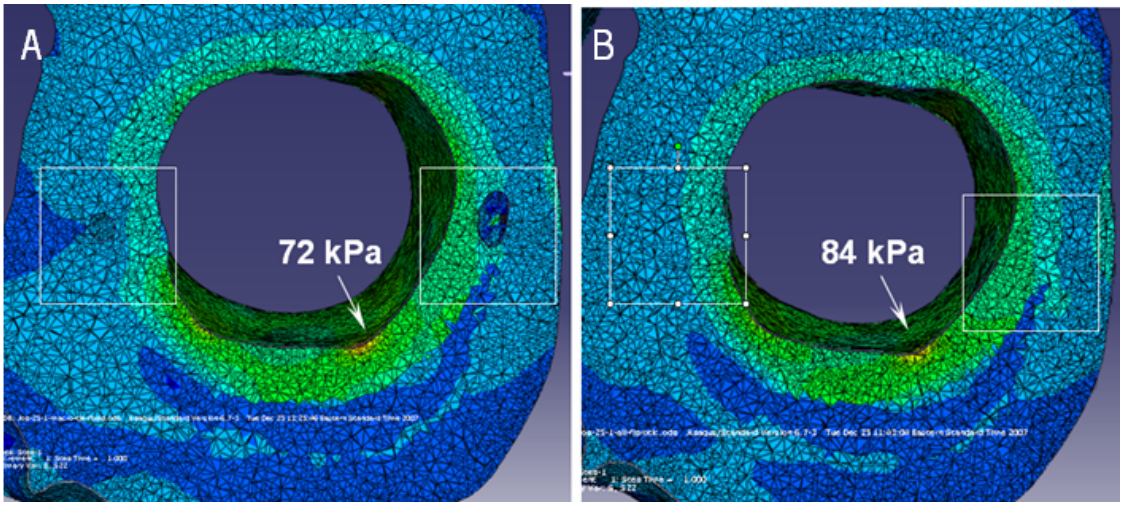

Figure 3-3. Circumferential stress distribution within the cross section. Maximum circumferential stress of 84 kPa without shoulder calcifications in B is reduced to 72 kPa in A in the presence of shoulders calcifications. Detailed stresses in the inserts are shown in Fig. 3-4 A and C.

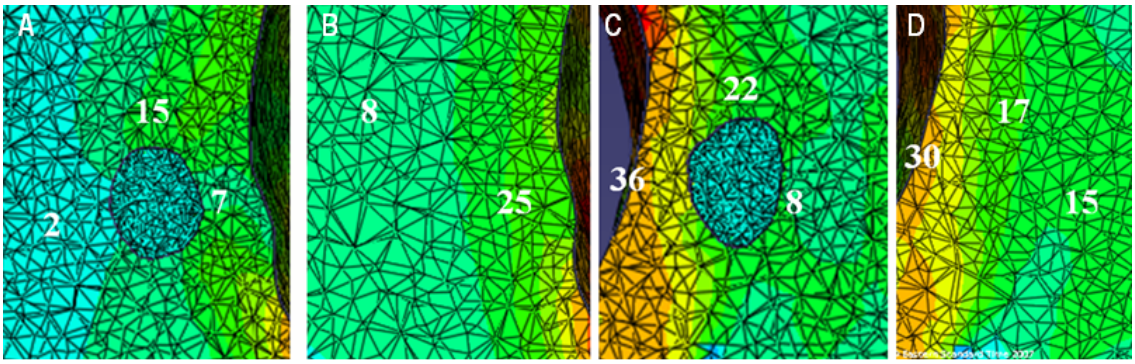

Figure 3-4. Local stress concentration around shoulder calcifications.

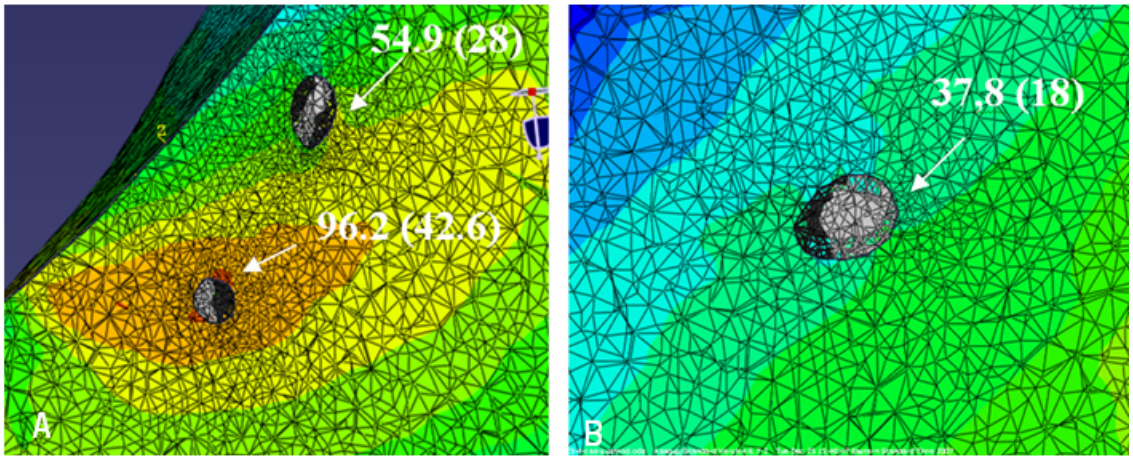

Figure 3-5. Stress concentration around microcalcifications in the thick fibrous cap of the original lesion circled in Fig. 3-1. Maximum local stress concentration (96.2 kPa) is higher than the global PCS in the same cap without microcalcifications.

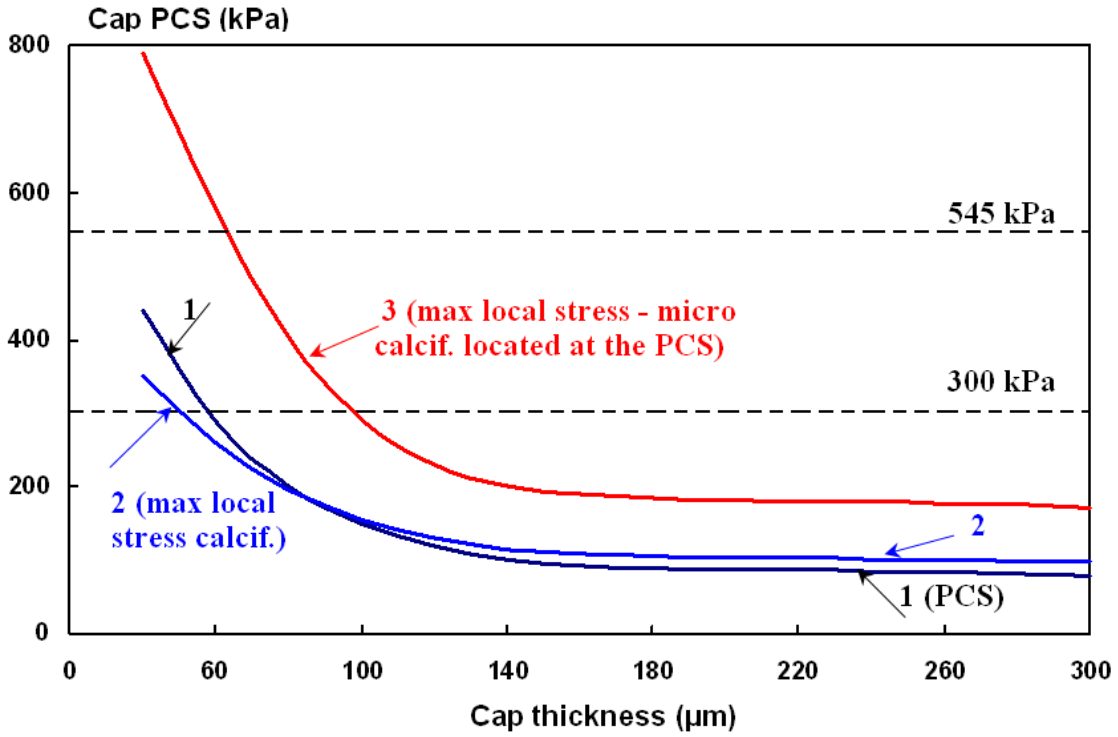

Figure 3-6. Global PCS in the fibrous cap (line 1) and maximum local stress around the original microcalcifications (line 2) in the "cap thinning" simulation. Line 3 corresponds to the maximum stresses around spherical microcalcifications located within the region of global PCS.

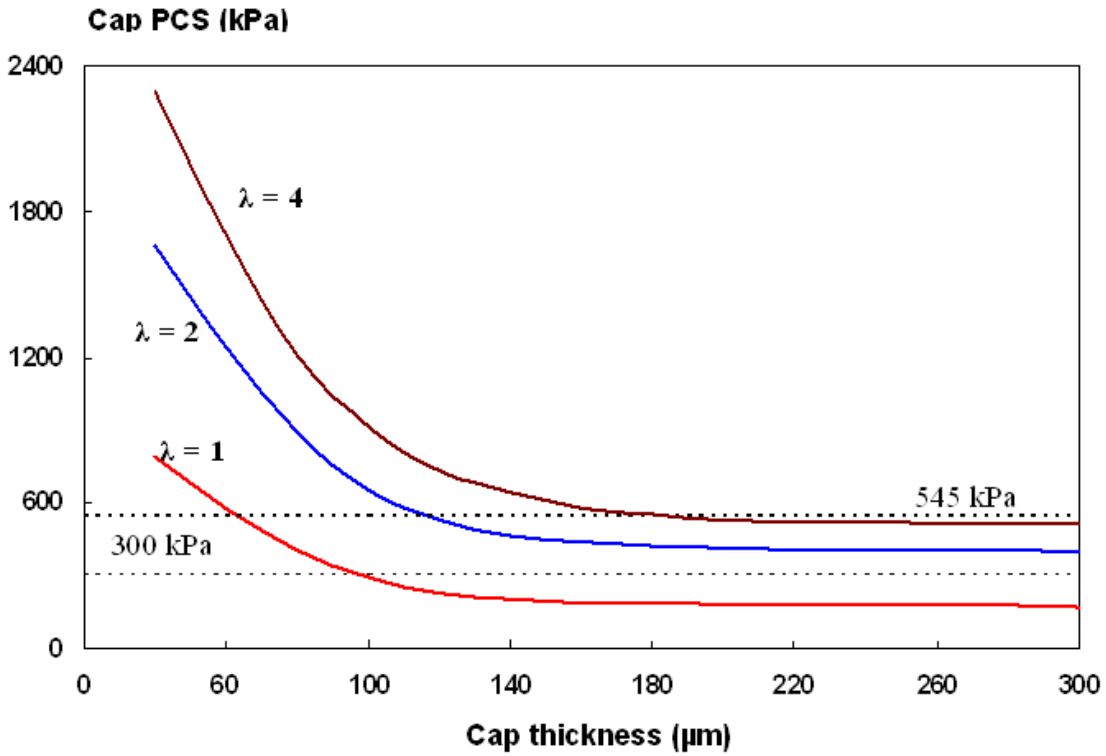

Figure 3-7. The effect of calcification shape at the cap PCS. Local maximum stress concentration around elliptical calcific inclusions located at the area of global PCS. Lines 1 - 3 correspond to the aspect ratios $\lambda = b/a = 1,2,4$.

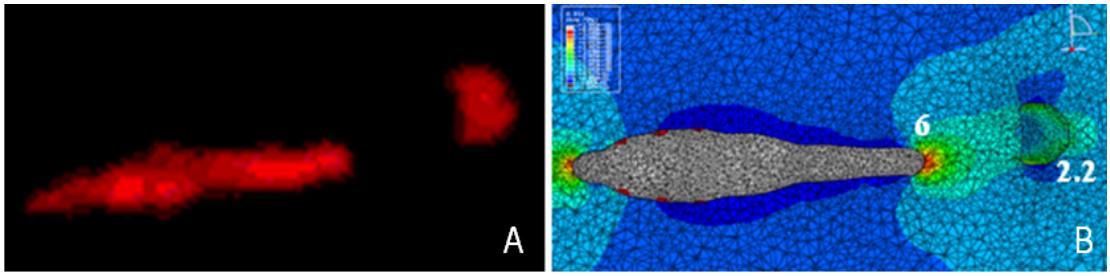

Figure 3-8. Stress concentration in a fibrous cap due to the presence of two adjacent calcifications stained with Alizarin Red S (A). An area of high circumferential stress is observed between the inclusions with a stress concentration of 6 at the pole of the elongated inclusion (B).

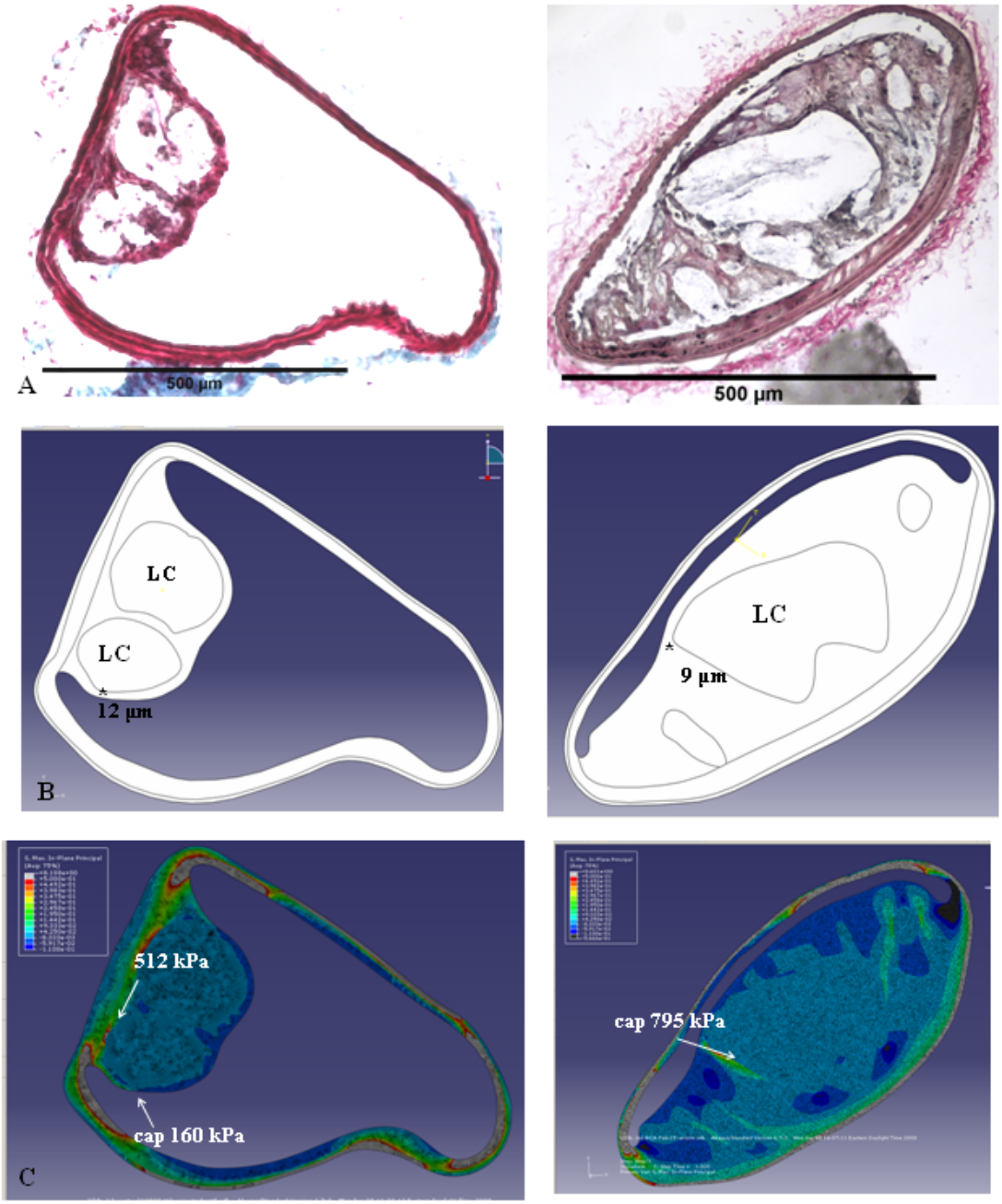

Figure 4-1. Histology based FEA of murine aortic (left panel) and BCA (right panel) lesions. (A) Advanced aortic and BCA lesions with fibrous caps and lipid cores stained with hematoxylin & eosin and Van Gieson stain. (B) Tracings identify regions of fibrous plaque, lipid, media, and adventitia. (C) Peak circumferential stress in the aortic lesion reaches 160 kPa (left panel), while maximum BCA cap stress is 795 kPa (right panel)

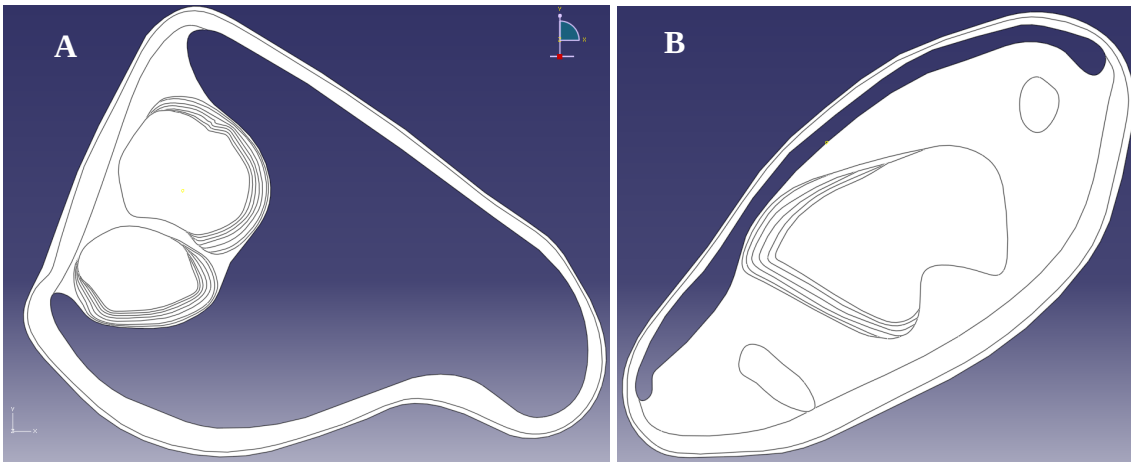

Figure 4-2. Idealized models of aortic (A) and brachiocephalic (B) murine lesion with cap thickness varying from varying from 25 micron to 2 micron for the "cap thinning" simulation shown in Fig. 4-3.

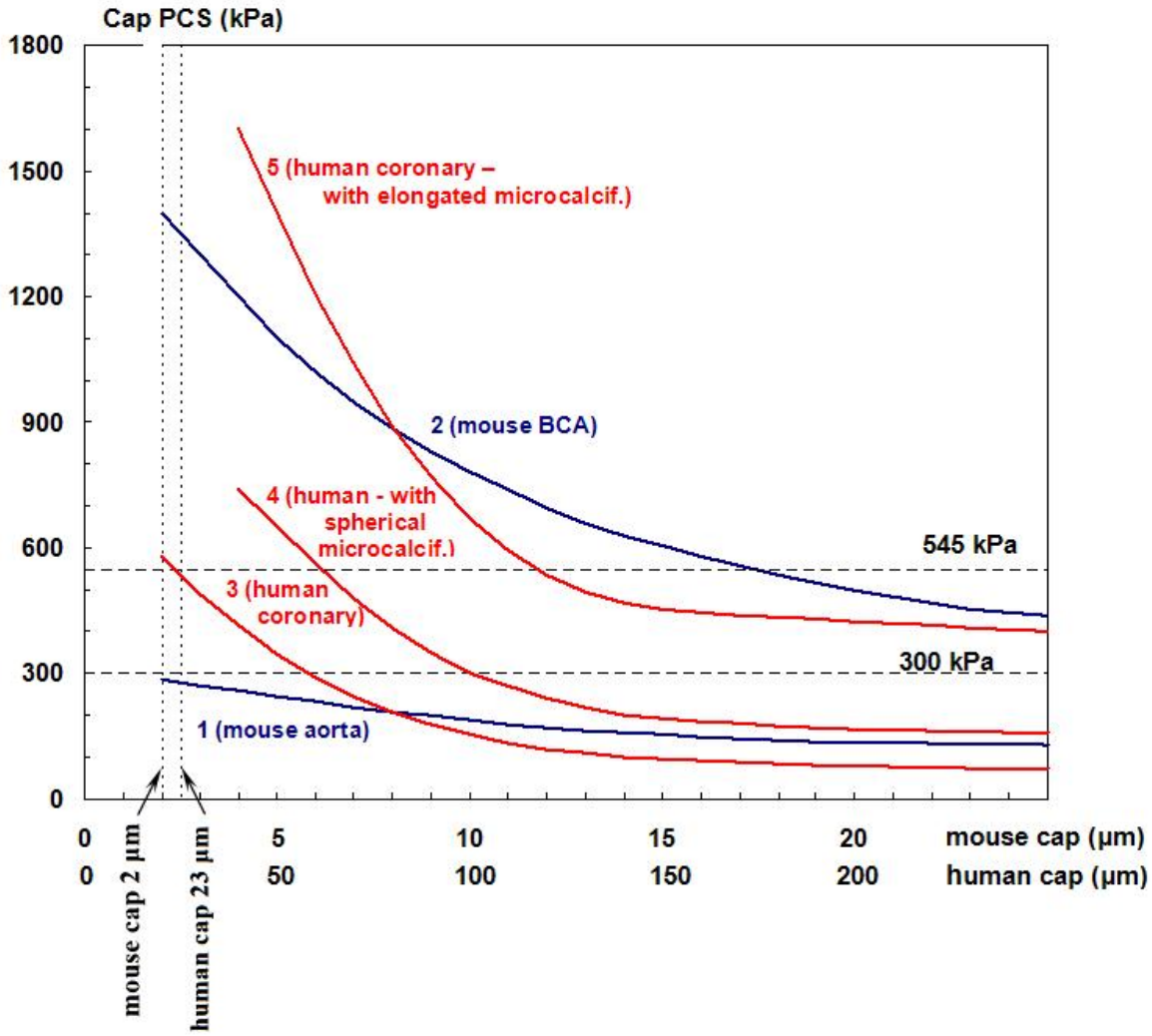

Figure 4-3. PCS in the fibrous cap of murine aortic (line 1) and BCA lesion (line 2) as a function of cap thickness. For comparison, we plotted PCS within a human coronary lesion: line 3 corresponds to the global PCS in the fibrous cap without microcalcifications, line 4 and 5 show how this stress would change if a spherical or an elongated microcalcification was located within the region of the PCS (lines 1 and 3 from Figure 3-6, line 2 from Figure 3-7).

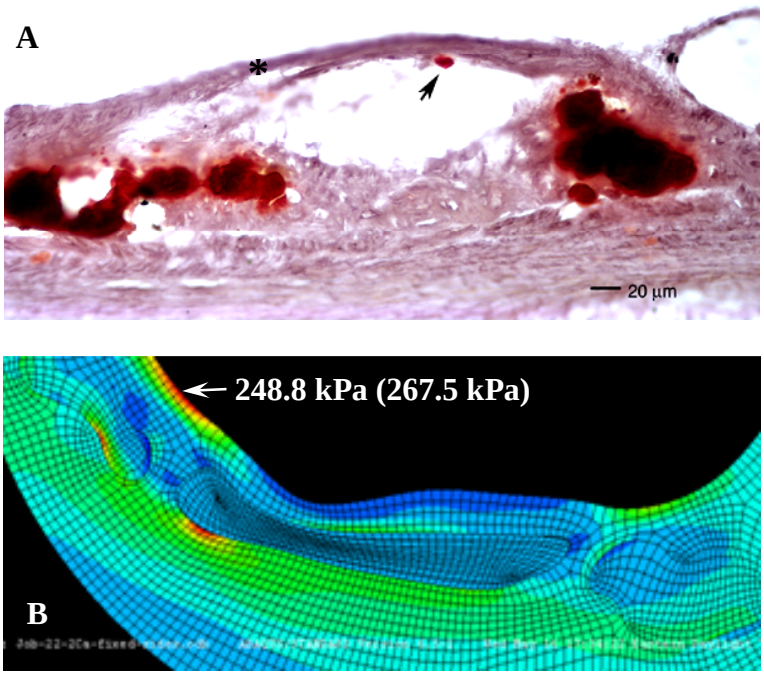

Figure 4-4. Stabilizing effect of large shoulder calcifications on aortic plaque stability. (A) Alizarin red staining of an aortic arch lesion in a 60-week old apoE KO female mouse, no counterstaining. (B) Finite element model of the lesion predicts maximum tensile stress of 248.8 kPa at the plaque shoulders where cap thickness is minimum (marked by an asterisk in A). The peak stress in the cap slightly increased reaching 267.5 kPa after two macrocalcifications has been replaced by fibrotic tissue.

Appendix A Stresses and displacements in a fibrous cap containing a perfectly bonded rigid spherical inclusion

1. Stress functions

A general solution of the equations (1) - (4) is represented as a combination of six harmonic functions $\phi_0, \phi_1, \phi_2, \phi_3, \phi_4, \lambda_3$. Components of the displacement vector $\mathbf{u}(u_x, v_y, w_z)$ are expressed in terms of these functions as follows:

$$2Gu_x = \frac{\partial \phi_0}{\partial x},\ 2Gv_y = \frac{\partial \phi_0}{\partial y},\ 2Gw_z = \frac{\partial \phi_0}{\partial z}$$

$$2Gu_x = x\frac{\partial \phi_1}{\partial x} - (3-4\nu)\phi_1,\ 2Gv_y = x\frac{\partial \phi_1}{\partial y},\ 2Gw_z = x\frac{\partial \phi_1}{\partial z}$$

$$2Gu_x = y\frac{\partial \phi_2}{\partial x},\ 2Gv_y = y\frac{\partial \phi_2}{\partial y} - (3-4\nu)\phi_2,\ 2Gw_z = y\frac{\partial \phi_2}{\partial z}$$

$$2Gu_x = z\frac{\partial \phi_3}{\partial x},\ 2Gv_y = z\frac{\partial \phi_3}{\partial y},\ 2Gw_z = z\frac{\partial \phi_3}{\partial z} - (3-4\nu)\phi_3 \qquad (5)$$

$$2Gu_x = x\frac{\partial \phi_4}{\partial x},\ 2Gv_y = y\frac{\partial \phi_4}{\partial z},\ 2Gw_z = -x\frac{\partial \phi_4}{\partial x} - y\frac{\partial \phi_4}{\partial y} - 4(1-\nu)\phi_4$$

$$2Gu_x = 2\frac{\partial \lambda_3}{\partial y},\ 2Gv_y = -2\frac{\partial \lambda_3}{\partial x},\ w_z = 0$$

where

$$\Delta^2\phi_0 = \Delta^2\phi_1 = \Delta^2\phi_2 = \Delta^2\phi_3 = \Delta^2\phi_4 = \Delta^2\lambda_3 = 0, \qquad (6)$$

$$\Delta^2 = \frac{\partial^2}{\partial x^2} + \frac{\partial^2}{\partial y^2} + \frac{\partial^2}{\partial z^2},$$

and ν and G denote Poisson's ratio and the shear modulus respectively. The displacement and stress fields derived from these harmonic stress functions satisfy the governing equation (1) in the absence of body forces.

2. Solution of the problem in the absence of an inclusion.

First we choose harmonic functions ϕ_0 and ϕ_3 in the following form:

$$\phi_0 = \frac{T_0}{4}\frac{1-\nu}{1+\nu}(x^2+y^2-2z^2)+\frac{T_0}{4}(x^2-y^2)= \\ -\frac{T_0}{2}\frac{1-\nu}{1+\nu}r^2P_2(\mu)+\frac{T_0}{12}r^2P_2^2(\mu)\cos(2\phi) \qquad (7)$$

$$\phi_3 = -\frac{T_0}{2(1+\nu)}z = -\frac{T_0}{2(1+\nu)}rP_1(\mu),$$

where $\mu=\cos\theta$; $P_n(\mu)$ and $P_n^m(\mu)$ are Legendre functions of the first kind of order n and associated Legendre function of the first kind of order n and degree m, respectively. Substituting expressions (7) for harmonic functions ϕ_0 and ϕ_3 into expressions (5) one can calculate the corresponding displacement and stress fields:

$$u_x = \frac{T_0}{E}x,\ v_y = -\frac{\nu T_0}{E}y,\ w_z = -\frac{\nu T_0}{E} \qquad (8)$$

$$\sigma_x = T_0,\ \sigma_y = \sigma_z = \tau_{xy} = \tau_{xz} = \tau_{yz} = 0\ , \qquad (9)$$

where E is Young's modulus.

Expressions (8), (9) represent a solution of the problem of a thick plate under uniaxial tension T_0 parallel to the x axis in the absence of an inclusion.

Equation (9) shows that this solution gives no traction at the surfaces of the plate $z = \pm 1 + c$. The components of the displacement on the inclusion surface are:

$$\left(u_r\right)_{r=a} = \frac{T_0 a}{2E}\left\{\left((1+\nu)\sin^2\theta - 2\nu\right) + (1+\nu)\sin^2\theta\cos 2\phi\right\}$$

$$\left(u_\theta\right)_{r=a} = \frac{T_0 a}{2E}(1+\nu)\sin\theta\cos\theta(1+\cos 2\phi) \qquad (10)$$

$$\left(u_\phi\right)_{r=a} = -\frac{T_0 a}{2E}(1+\nu)\sin\theta\sin 2\phi$$

In order to satisfy zero displacement boundary conditions at the inclusion interface (3) when an inclusion is present, we construct auxiliary stress functions using suitable harmonic functions such that they would yield no traction on the plate surfaces

$$(\sigma_z)_{z=\pm 1+c} = (\tau_{\rho z})_{z=\pm 1+c} = (\tau_{\varphi z})_{z=\pm 1+c} = 0 \qquad (11)$$

and satisfy following boundary conditions at $r = a$:

$$\left(u_r\right)_{r=a} = -\frac{T_0 a}{2E}\left\{\left((1+\nu)\sin^2\theta - 2\nu\right) + (1+\nu)\sin^2\theta\cos 2\phi\right\}$$

$$\left(u_\theta\right)_{r=a} = -\frac{T_0 a}{2E}(1+\nu)\sin\theta\cos\theta(1+\cos 2\phi) \qquad (12)$$

$$\left(u_\phi\right)_{r=a} = \frac{T_0 a}{2E}(1+\nu)\sin\theta\sin 2\phi \qquad (13)$$

Expressions (11)-(13) are split into an axisymmetric part which doesn't depend on φ and an asymmetric part which is a function of φ.

3. Axisymmetric solution

First we construct the auxiliary stress functions for the case of a stress distribution which is axisymmetric about the z axis as follows:

$$\phi_0 = T_0 \sum_{m=0}^{\infty} A_m \frac{P_m(\mu)}{r^{m+1}},\ \phi_3 = T_0 \sum_{m=0}^{\infty} B_m \frac{P_m(\mu)}{r^{m+1}} \tag{14}$$

where A_m, B_m are unknown coefficients of the spherical stress functions, $\boldsymbol{P_m(\mu)}$ are Legendre functions and

$$\phi_0 = T_0 \int_0^{\infty} \psi_1(\lambda) J_0(\lambda\rho) \cosh \lambda z d\lambda,\ \phi_3 = T_0 \int_0^{\infty} \lambda \psi_2(\lambda) J_0(\lambda\rho) \sinh \lambda z d\lambda \tag{15}$$

$$\phi_0 = T_0 \int_0^{\infty} \psi_1^*(\lambda) J_0(\lambda\rho) \sinh \lambda z d\lambda,\ \phi_3 = T_0 \int_0^{\infty} \lambda \psi_2^*(\lambda) J_0(\lambda\rho) \cosh \lambda z d\lambda$$

where $J_0(\lambda\rho)$ is a Bessel function of the first kind of the zero order and $\psi_1(\lambda), \psi_2(\lambda), \psi_1^*(\lambda), \psi_2^*(\lambda)$ are arbitrary cylindrical functions of λ.

The following integral relation

$$\frac{P_n^m(\mu)}{r^{m+1}} = \frac{1}{(m-n)!} \int_0^{\infty} \lambda^m J_n(\lambda\rho) e^{-\lambda z} d\lambda \ (z > 0) \tag{16}$$

allows one to express the spherical stress functions (14) in cylindrical coordinates and rewrite the stress-free boundary conditions at $z = \pm 1 + c$ (11) as follows:

$$\left(\frac{\sigma_z}{T_0}\right)_{z=\pm 1+c} = \int_0^{\infty} \lambda^2 [\psi_1(\lambda) \cosh(1 \pm c)\lambda + ((1 \pm c)\lambda \sinh(1 \pm c)\lambda - 2(1-\nu)\cosh(1 \pm c)\lambda)\psi_2(\lambda)\ \mu$$
$$\psi_1^*(\lambda) \sinh(1 \pm c)\lambda\ \mu\ ((1 \pm c)\lambda \cosh(1 \pm c)\lambda - 2(1-\nu)\sinh(1 \pm c)\lambda)\psi_2^*(\lambda) +$$
$$\sum_{m=0}^{\infty} \left(\frac{A_{2m}}{(2m)!} \lambda^{2m} \pm \frac{A_{2m+1}}{(2m+1)!} \lambda^{2m+1} \right) e^{-(1 \pm c)\lambda} + \sum_{m=0}^{\infty} \left(\pm \frac{B_{2m}}{(2m)!} \lambda^{2m-1} \pm \frac{B_{2m+1}}{(2m+1)!} \lambda^{2m+1} \right) \times$$
$$(2(1-\nu) + (1 \pm c)\lambda) e^{-(1 \pm c)\lambda}] J_0(\lambda\rho) d\lambda = 0$$

$$\left(\frac{\tau_{\rho z}}{T_0}\right)_{z=\pm 1+c} = \int_0^\infty \lambda^2 [\psi_1(\lambda)\sinh(1\pm c)\lambda - ((1-2\nu)\sinh(1\pm c)\lambda - (1\pm c)\lambda\cosh(1\pm c)\lambda)\psi_2(\lambda)\,\mu$$

$$\psi_1^*(\lambda)\cosh(1\pm c)\lambda\,\mu\,((1-2\nu)\cosh(1\pm c)\lambda - (1\pm c)\lambda\sinh(1\pm c)\lambda)\psi_2^*(\lambda) -$$

$$\sum_{m=0}^{\infty}\left(\frac{A_{2m}}{(2m)!}\lambda^{2m} \pm \frac{A_{2m+1}}{(2m+1)!}\lambda^{2m+1}\right)e^{-(1\pm c)\lambda} + \sum_{m=0}^{\infty}\left(\pm\frac{B_{2m}}{(2m)!}\lambda^{2m-1} \pm \frac{B_{2m+1}}{(2m+1)!}\lambda^{2m+1}\right)\times$$

$$((1-2\nu)+(1\pm c)\lambda)e^{-(1\pm c)\lambda}]J_1(\lambda\rho)d\lambda = 0 \qquad (17)$$

The next step is to express cylindrical functions $\psi_1, \psi_1^*, \psi_2, \psi_2^*$ in terms of the spherical functions (14) by applying Hankel transforms to the stress free boundary conditions (17) and solving the four linear algebraic equations simultaneously for $\psi_1, \psi_1^*, \psi_2, \psi_2^*$:

$$\psi_1(\lambda) = \frac{1}{F(\lambda)}\sum_{m=0}^{\infty}\frac{A_{2m}}{(2m)!}\lambda^{2m}((3-4\nu-2\lambda)(\sinh 2\lambda\cosh 2\lambda c - 2\lambda) + e^{-2\lambda}(\sinh 2\lambda - 2\lambda\cosh 2\lambda c) +$$

$$2c\lambda\sinh 2\lambda\sinh 2\lambda c) + \sum_{m=0}^{\infty}\frac{A_{2m+1}}{(2m+1)!}\lambda^{2m+1}((3-4\nu-2\lambda)(\sinh 2\lambda\sinh 2\lambda c - 2\lambda e^{-2\lambda}\sinh 2\lambda c +$$

$$2c\lambda(\sinh 2\lambda\cosh 2\lambda c + 2\lambda) + \sum_{m=0}^{\infty}\frac{B_{2m}}{(2m)!}\lambda^{2m-1}((4(1-\nu)(1-2\nu)-2\lambda^2)\sinh 2\lambda\sinh 2\lambda c +$$

$$4\lambda^2 c((3-4\nu)+\cosh 2\lambda\cosh 2\lambda c) - 2\lambda^2 c^2\sinh 2\lambda\sinh 2\lambda c) + \sum_{m=0}^{\infty}\frac{B_{2m+1}}{(2m+1)!}\times$$

$$\lambda^{2m}((4(1-\nu)(1-2\nu)-2\lambda^2)(\sinh 2\lambda\cosh 2\lambda c - 2\lambda) + 4\lambda^2 c(\cosh 2\lambda\sinh 2\lambda c - \lambda c) -$$

$$2\lambda^2 c^2\sinh 2\lambda\cosh 2\lambda c)$$

$$\psi_1^*(\lambda) = \frac{1}{F(\lambda)}\sum_{m=0}^{\infty}\frac{A_{2m}}{(2m)!}\lambda^{2m}((3-4\nu-2\lambda)(\sinh 2\lambda\sinh 2\lambda c - 2\lambda e^{-2\lambda}\sinh 2\lambda c + 2\lambda c(\sinh 2\lambda\times$$

$$\cosh 2\lambda c - 2\lambda) + \sum_{m=0}^{\infty} \frac{A_{2m+1}}{(2m+1)!} \lambda^{2m+1}((3-4\nu-2\lambda)(\sinh 2\lambda \cosh 2\lambda c + 2\lambda) - e^{-2\lambda}(\sinh 2\lambda +$$

$$2\lambda \cosh 2\lambda c) + 2\lambda c \sinh 2\lambda \sinh 2\lambda c) + \sum_{m=0}^{\infty} \frac{B_{2m}}{(2m)!} \lambda^{2m-1}((4(1-\nu)(1-2\nu) - 2\lambda^2)(\sinh 2\lambda$$

$$\cosh 2\lambda c + 2\lambda) + 4\lambda^2 c \cosh 2\lambda \sinh 2\lambda c - 2\lambda^2 c^2 (\sinh 2\lambda \cosh 2\lambda c - 2\lambda) + \sum_{m=0}^{\infty} \frac{B_{2m+1}}{(2m+1)!} \lambda^{2m} \times$$

$$2\lambda^2 c^2 \sinh 2\lambda \cosh 2\lambda c)$$

$$\psi_2(\lambda) = \frac{1}{F(\lambda)} \sum_{m=0}^{\infty} \frac{2A_{2m}}{(2m)!} \lambda^{2m} (\sinh 2\lambda \cosh 2\lambda c - 2\lambda) + \sum_{m=0}^{\infty} \frac{2A_{2m+1}}{(2m+1)!} \lambda^{2m+1} \sinh 2\lambda \sinh 2\lambda c +$$

$$2c\lambda(\sinh 2\lambda \cosh 2\lambda c + 2\lambda) + \sum_{m=0}^{\infty} \frac{B_{2m}}{(2m)!} \lambda^{2m-1}((3-4\nu+2\lambda)\sinh 2\lambda \sinh 2\lambda c +$$

$$2\lambda e^{-2\lambda} \sinh 2\lambda c - 2\lambda c(\sinh 2\lambda \cosh 2\lambda c - 2\lambda)) + \sum_{m=0}^{\infty} \frac{B_{2m+1}}{(2m+1)!} \lambda^{2m}((3-4\nu+2\lambda) \times$$

$$(\sinh 2\lambda \cosh 2\lambda c - 2\lambda) - e^{-2\lambda}(\sinh 2\lambda - 2\lambda \cosh 2\lambda c) - 2\lambda c \sinh 2\lambda \sinh 2\lambda c)$$

$$\psi_2^*(\lambda) = \frac{1}{F(\lambda)} \sum_{m=0}^{\infty} \frac{2A_{2m}}{(2m)!} \lambda^{2m} \sinh 2\lambda \cosh 2\lambda c + \sum_{m=0}^{\infty} \frac{2A_{2m+1}}{(2m+1)!} \lambda^{2m+1}(\sinh 2\lambda \cosh 2\lambda c + 2\lambda) +$$

$$\sum_{m=0}^{\infty} \frac{B_{2m}}{(2m)!} \lambda^{2m-1}((3-4\nu+2\lambda)(\sinh 2\lambda \cosh 2\lambda c + 2\lambda) + e^{-2\lambda}(\sinh 2\lambda + 2\lambda \cosh 2\lambda c) -$$

$$2\lambda c \sinh 2\lambda \sinh 2\lambda c) + \sum_{m=0}^{\infty} \frac{B_{2m+1}}{(2m+1)!} \lambda^{2m}((3-4\nu+2\lambda)\sinh 2\lambda \sinh 2\lambda c +$$

$$2\lambda e^{-2\lambda} \sinh 2\lambda c - 2\lambda c(\sinh 2\lambda \cosh 2\lambda c + 2\lambda)$$

(18)

where

$$F(\lambda) = \sinh^2 2\lambda - 4\lambda^2$$

To satisfy remaining boundary conditions at the inclusion interface (12) one has to express the cylindrical functions (15) in spherical coordinates using following relations:

$$J_\nu(k\rho)\cosh kz = \sum_{n=0}^{\infty} \frac{k^{\nu+2n}}{(2\nu+2n)!} r^{\nu+2n} P_{\nu+2n}^{\nu}(\mu)$$

(19)

$$J_\nu(k\rho)\sinh kz = \sum_{n=0}^{\infty} \frac{k^{\nu+2n+1}}{(2\nu+2n+1)!} r^{\nu+2n+1} P_{\nu+2n+1}^{\nu}(\mu)$$

The resulting expansions of the cylindrical functions φ_0 and φ_3 (15) are given by

$$\phi_0 = T_0 \sum_{n=0}^{\infty} a_n r^n P_n(\mu), \quad \phi_3 = T_0 \sum_{n=0}^{\infty} b_n r^n P_n(\mu)$$

(20)

where coefficients a_n and b_n are determined by

$$a_{2n} = \frac{1}{(2n)!} \int_0^{\infty} \psi_1(\lambda)\lambda^{2n} d\lambda, \quad a_{2n+1} = \frac{1}{(2n+1)!} \int_0^{\infty} \psi_1^*(\lambda)\lambda^{2n+1} d\lambda,$$

(21)

$$b_{2n} = \frac{1}{(2n)!} \int_0^{\infty} \psi_2^*(\lambda)\lambda^{2n+1} d\lambda, \quad b_{2n+1} = \frac{1}{(2n+1)!} \int_0^{\infty} \psi_2(\lambda)\lambda^{2n+2} d\lambda.$$

Substituting $\psi_1(\lambda), \psi_2(\lambda), \psi_1^*(\lambda), \psi_2^*(\lambda)$ given by (18) into equations (21), one obtains expressions for a_n and b_n can be obtained in terms of the unknown spherical

coefficients A_n, B_n. These expressions contain integrals with respect to λ which have to be evaluated numerically.

Finally, using stress functions (5) and satisfying boundary conditions (10), one can obtain the resulting system for the axisymmetric case

$$\sum_{n=0}^{\infty}\left(-(n+1)\frac{A_n}{a^{n+2}}-\frac{(n+3-4\nu)n}{2n-1}\frac{B_{n-1}}{a^n}-\frac{(n+1)(n+5-4\nu)}{2n+3}\frac{B_{n+1}}{a^{n+2}}+n\alpha_n a^{n-1}+\right.$$

$$\left.\frac{n(n-4+4\nu)}{2n-1}\beta_{n-1}a^{n-1}+\frac{(n+1)(n-2+4\nu)}{2n+3}\beta_{n+1}a^{n+1}\right)P_n=-\frac{1-2\nu}{3(1+\nu)}aP_0+\frac{a}{3}P_2$$

(22)

$$\sum_{n=1}^{\infty}\left(\frac{A_n}{a^{n+2}}+\frac{(n-4+4\nu)}{2n-1}\frac{B_{n-1}}{a^n}+\frac{(n+5-4\nu)}{2n+3}\frac{B_{n+1}}{a^{n+2}}+\alpha_n a^{n-1}+\right.$$

$$\left.\frac{n-4+4\nu}{2n-1}\beta_{n-1}a^{n-1}+\frac{n+5-4\nu}{2n+3}\beta_{n+1}a^{n+1}\right)P_n'\sin\theta=\frac{1}{2}aP_2'\sin\theta$$

(23)

Equating coefficients of each Legendre function $P_n(\mu)$ in equation (22) or its derivative $P_n'(\mu)$ in equation (23) to zero, one obtains a system of linear equations for the unknown coefficients of the spherical harmonics A_n, B_n. The axisymmetric solution of the problem (1) - (4) is determined by truncating and solving this system. After solving for the coefficients, one can calculate the stresses and deformations at any point within the plate.

4. Asymmetric solution

For the asymmetric problem, the pure shear spherical and cylindrical harmonics are defined by

$$\phi_0 = T_0 \sum_{m=2}^{\infty} C_m \frac{P_m^2(\mu)}{r^{m+1}} \cos 2\phi, \qquad \phi_1 = T_0 \sum_{m=2}^{\infty} C_m \frac{P_m^1(\mu)}{r^{m+1}} \cos \phi,$$

$$\phi_2 = -T_0 \sum_{m=2}^{\infty} D_m \frac{P_m^1(\mu)}{r^{m+1}} \sin \phi$$

$$\phi_3 = T_0 \sum_{m=2}^{\infty} E_m \frac{P_m^2(\mu)}{r^{m+1}} \cos 2\phi, \ \phi_4 = -T_0 \sum_{m=2}^{\infty} \frac{D_m}{(m-1)} \frac{P_m^2(\mu)}{r^{m+1}} \cos 2\phi$$

(24)

$$\phi_0 = T_0 \int_0^{\infty} \varphi_3(\lambda) J_2(\lambda\rho) \cosh \lambda z \cos 2\phi d\lambda, \ \phi_1 = T_0 \int_0^{\infty} \varphi_4(\lambda) J_1(\lambda\rho) \cosh \lambda z \cos \phi d\lambda$$

$$\phi_2 = -T_0 \int_0^{\infty} \varphi_4(\lambda) J_1(\lambda\rho) \cosh \lambda z \sin \phi d\lambda, \ \phi_3 = T_0 \int_0^{\infty} \lambda\varphi_5(\lambda) J_2(\lambda\rho) \sinh \lambda z \cos 2\phi d\lambda$$

$$\lambda_3 = T_0 \int_0^{\infty} \varphi_6(\lambda) J_2(\lambda\rho) \cosh \lambda z \sin 2\phi d\lambda$$

(25)

$$\phi_0 = T_0 \int_0^{\infty} \varphi_3^*(\lambda) J_2(\lambda\rho) \sinh \lambda z \cos 2\phi d\lambda, \ \phi_1 = T_0 \int_0^{\infty} \varphi_4^*(\lambda) J_1(\lambda\rho) \sinh \lambda z \cos \phi d\lambda$$

$$\phi_2 = -T_0 \int_0^{\infty} \varphi_4^*(\lambda) J_1(\lambda\rho) \sinh \lambda z \sin \phi d\lambda, \ \phi_3 = T_0 \int_0^{\infty} \lambda\varphi_5^*(\lambda) J_2(\lambda\rho) \sinh \lambda z \cos 2\phi d\lambda$$

$$\lambda_3 = T_0 \int_0^{\infty} \varphi_6^*(\lambda) J_2(\lambda\rho) \sinh \lambda z \sin 2\phi d\lambda,$$

where C_n, D_n and E_n are unknown coefficients of the spherical harmonics; $\psi_3(\lambda), \psi_4(\lambda), \psi_5(\lambda), \psi_6(\lambda)$ and $\psi_3^*(\lambda), \psi_4^*(\lambda), \psi_5^*(\lambda), \psi_6^*(\lambda)$ are arbitrary functions.

In a similar procedure to that described in the previous section, one satisfies boundary conditions (11) and (12) by using relations (16) and (19). The final equations for the asymmetric case are

$$\sum_{n=2}^{\infty}\Bigg(-(n+1)\frac{C_n}{a^{n+2}}-\frac{5-4\nu}{3}\frac{D_1}{a^2}\delta_n^{(2)}+\frac{2(1-2\nu)}{n}\frac{D_{n-1}}{a^{n+2}}-\frac{(n-2)(n+3-4\nu)}{2n-1}\frac{E_{n-1}}{a^n}-$$

$$\frac{(n+3)(n+5-4\nu)}{2n+3}\frac{E_{n+1}}{a^{n+2}}+n\xi_n a^{n-1}+\frac{n-4+4\nu}{2n-1}\eta_{n-1}a^{n-1}-\frac{n-2+4\nu}{2n+3}\eta_{n+1}a^{n+1}+$$

$$\frac{(n-2)(n-4+4\nu)}{2n-1}\varsigma_{n-1}a^{n-1}+\frac{(n+3)(n-2+4\nu)}{2n+3}\varsigma_{n+1}a^{n+1}+4k_n a^{n-1}\Bigg)P_n^2(\mu)=-\frac{a}{6}P_2^2$$

$$\sum_{n=2}^{\infty}\Bigg(-\frac{C_n}{a^{n+2}}-\frac{1-2\nu}{2n+3}\frac{D_{n+1}}{a^{n+2}}+\frac{1-2\nu}{2n-1}\frac{D_{n-1}}{a^n}-\frac{n-2}{2n-1}\frac{E_{n-1}}{a^n}-\frac{n+3}{2n+3}\frac{E_{n+1}}{a^{n+2}}-$$

(26)

$$\xi_n a^{n-1}-\frac{1-2\nu}{2n-1}\eta_{n-1}a^{n-1}+\frac{1-2\nu}{2n+3}\eta_{n+1}a^{n+1}-\frac{n-2}{2n-1}\varsigma_{n-1}a^{n-1}-\frac{n+3}{2n+3}\varsigma_{n+1}a^{n+1}-$$

$$\frac{n(n-1)+4}{2n-1}k_n a^{n-1}+\frac{(n+3)(n+4)}{2n+3}k_{n+2}a^{n+1}\Bigg)P_n^2(\mu)=\frac{a}{12}P_2^2$$

$$\sum_{n=2}^{\infty}\Bigg(-\frac{(1-2\nu)(n+1)}{n-1}\frac{D_n}{a^{n+1}}+4(1-\nu)\frac{E_n}{a^{n+1}}-2(1-\nu)\eta_n a^n+4(1-\nu)\varsigma_n a^n+$$

$$n(n+3)k_{n+1}a^n\Bigg)P_n^2(\mu)=0$$

Equating coefficients of each Legendre function $P_n^2(\mu)$ in equation (26) to zero, one obtains a system of linear equations. The asymmetric solution of equations (1) - (4) is determined by solving the linear simultaneous equations for the parametric coefficients of the spherical harmonics C_n, D_n, E_n. Solving for the coefficients, one can calculate the stresses and deformations corresponding to the asymmetric case at any point within the plate.

5. The combined solution

Final expressions for the displacement and stress fields are given by

$$u = u_1 + u_2 \cos 2\varphi, \qquad \sigma_i = \sigma_{i1} + \sigma_{i2} \cos 2\varphi,$$

where $\mathbf{u_1}$, σ_{i1} and $\mathbf{u_2}$, σ_{i2} represent the axisymmetric and the symmetric parts respectively.

Bibliography

1. Altenburg, M., Homeister, J., Doherty, H., Maeda, N. (2004) “Genetics of atherosclerosis in murine models.” *Curr Drug Targets.* **8**(11):1161-1171.

2. Beckman, J.A., Ganz, J., Creager, M.A., Ganz, P., Kinlay, S. (2001) “Relationship of clinical presentation and calcification of culprit coronary artery stenoses.” *Arterioscler Thromb Vasc Biol.* **21**: 1618 –22.

3. Bennett, B. J., Scatena, M., Kirk, E. A., Rattazzi, M., Varon, R. M., Averill, M., Schwartz, S. M., Giachelli, C. M., and Rosenfeld, M. E. (2006) "Osteoprotegerin inactivation accelerates advanced atherosclerotic lesion progression and calcification in older ApoE-/- mice." *Arterioscler Thromb Vasc Biol* **26**: 2117-2124.

4. Bernacca, G.M., Gibson, S.A., Wilkinson, R., Wheatley, D.J. (1994) "Confocal laser scanning microscopy of calcified bioprosthetic heart valves." *J Heart Valve Dis*. **3**:205–211.

5. Breslow, J. L. (1996) "Mouse models of atherosclerosis." *Science* **272:** 685-688.

6. Burke, A.P., Farb, A., Malcom, G.T., Liang, Y.H., Smialek, J., Virmani, R. (1997) "Coronary risk factors and plaque morphology in men with coronary disease who died suddenly." *N Engl J Med.* **336:**1276–1282.

7. Burke, A.P., Farb, A., Malcom, G.T., Liang, Y., Smialek, J.E., Virmani, R. (1999) "Plaque rupture and sudden death related to exertion in men with coronary artery disease." *J Am Med Assoc.* **281:**921–926.

8. Burke, A.P., Weber, D.K., Kolodgie, F.D., Farb, A., Taylor, A.J., Virmani, R.. (2001) "Pathophysiology of calcium deposition in coronary arteries." *Herz* **26**:239–44.

9. Calara, F., Silvestre, M., Casanada, F., Yuan, N., Napoli, C., and Palinski, W. (2001) "Spontaneous plaque rupture and secondary thrombosis in apolipoprotein E-deficient and LDL receptor-deficient mice." *J Pathol* **195***:* 257-263.

10. Chau, A.H., Chan, R.C. Shishkov, M., MacNeill, B., Iftimia, N., Tearney, G.J., Kamm, R.D., Bouma, B.E., Kaazempur-Mofrad, M.R. (2004) "Mechanical analysis of atherosclerotic plaques based on optical coherence tomography." *Ann. Biomed. Eng.* **32**(11): 1494–1503.

11. Cheng, G.C., Loree, H.M., Kamm, R.D., Fishbein, M.C., Lee, R.T. (1993) "Distribution of circumferential stress in ruptured and stable atherosclerotic

lesions. A structural analysis with histopathological correlation." *Circulation* **87**:1179-87.

12. Cheruvu, P.K., Finn, A.V., Gardner, C., Caplan, J., Goldstein, J., Stone, G.W., Virmani, R., Muller, J.E. (2007) "Frequency and distribution of thin-cap fibroatheroma and ruptured plaques in human coronary arteries: a pathologic study." *J Am Coll Cardiol.* **50**(10):940-949.

13. Daugherty, A. (2002) "Mouse models of atherosclerosis." *Am J Med Sci.* **323**(1):3-10.

14. Falk, E. (1992) "Why do plaques rupture?" *Circulation* **86**:III30-III42.

15. Finet, G., Ohayon, J., Rioufol, G. (2004) "Biomechanical interaction between cap thickness, lipid core composition and blood pressure in vulnerable coronary plaque: impact on stability or instability." *Coronary Artery Disease* **15**:13-20.

16. Friedrich, G.J., Moes, N.Y., Muhlberger, V.A., Gabl, C., Mikuz, G., Hausmann, D., Fitzgerald, P.J., Yock, P.G. (1994) "Detection of intralesional calcium by intracoronary ultrasound depends on the histologic pattern." *Am Heart J.* **128**:435–441.

17. Fujii, K., Carlier, S.G., Mintz, G.S., Takebayashi, H., Yasuda, T., Costa, R.A., Moussa, I., Dangas, G., Mehran, R., Lansky, A.J., Kreps, E.M., Collins, M., Stone, G.W., Moses, J.W., Leon, M.B. (2005) "Intravascular ultrasound study of patterns of calcium in ruptured coronary plaques." *Am J Cardiol.* **96**(3):352-7.

18. Ehara, S., Kobayashi, Y., Yoshiyama, M., Shimada, K., Shimada, Y., Fukuda, D., Nakamura, Y., Yamashita, H., Yamagishi, H., Takeuchi, K., *et al.* (2004) "Spotty calcification typifies the culprit plaque in patients with acute myocardial infarction: an intravascular ultrasound study." *Circulation* **110**: 3424-3429.

19. Gent, A. and Park, B. (1984) "Failure processes in elastomers at or near a rigid spherical inclusion." *J Mater Sci.* **19:** 1947–1956.

20. Glagov, S., Weisenberg, E., Zarins, C.K., Stankunavicius, R., Kolettis, G.J. (1987) "Compensatory enlargement of human atherosclerotic coronary arteries." *N Engl J Med.* **316**(22):1371-1375.

21. Glass, C. K. and Witztum, J. L. (2001) "Atherosclerosis: the road ahead." *Cell* **104**: 503-516.

22. Goodier, J. (1933) "Concentration of stress around spherical and cylindrical inclusions and flaws." *J Trans ASME* **55**: 39–44.

23. Greve, J.M., Les, A.S., Tang, B.T., Draney Blomme, M.T., Wilson, N.M., Dalman, R.L., Pelc, N.J., Taylor, C.A. (2006) "Allometric scaling of wall shear stress from mice to humans: quantification using cine phase-contrast MRI and computational fluid dynamics." *Am J Physiol Heart Circ Physiol.* **291**(4):H1700-1708.

24. Huang, H., Virmani, R., Younis, H., Burke, A. P., Kamm, R. D., and Lee, R. T. (2001) "The impact of calcification on the biomechanical stability of atherosclerotic plaques." *Circulation* **103**:1051-56.

25. Imoto, K, Hiro, T, Fujii, T, Murashige, A, Fukumoto, Y, Hashimoto, G, Okamura, T, Yamada, J, Mori, K and Matsuzaki, M. (2005) "Longitudinal Structural Determinants of Atherosclerotic Plaque Vulnerability." *J Am Coll Cardiol* **46:** 1507–1515.

26. Jackson, C.L., Bennett, M.R., Biessen, E.A., Johnson, J.L., Krams, R. (2007) "Assessment of unstable atherosclerosis in mice." *Arterioscler Thromb Vasc Biol.* **27**(4):714-720.

27. Jackson, C.L. (2007) "Defining and defending murine models of plaque rupture." *Arterioscler Thromb Vasc Biol.* **27**(4):973-977.

28. Jensen, L.O., Mintz, G.S., Carlier, S.G., Fujii, K., Moussa, I., Dangas, G., Mehran, R., Stone, G.W., Leon, M.B., Moses, J.W. (2006) "Intravascular ultrasound assessment of fibrous cap remnants after coronary plaque rupture." *Am Heart J.* **152**(2): 327-32.

29. Jin, X., Iwasa, S., Okada, K., Ooi, A., Mitsui, K., Mitsumata, M. (2003) "Shear stress-induced collagen XII expression is associated with atherogenesis." *Biochem Biophys Res Commun.* **308**(1):152-158.

30. Johnson, J. L., and Jackson, C. L. (2001) "Atherosclerotic plaque rupture in the apolipoprotein E knockout mouse." *Atherosclerosis* **154:** 399-406.

31. Johnson, J., Carson, K., Williams, H., Karanam, S., Newby, A., Angelini, G., George, S., and Jackson, C. (2005) "Plaque rupture after short periods of fat feeding in the apolipoprotein E-knockout mouse: model characterization and effects of pravastatin treatment." *Circulation* **111:** 1422-1430.

32. Kolodgie, F.D., Burke, A.P., Farb, A., Gold, H.K., Yuan, J., Narula, J., Finn, A.V., Virmani, R. (2001) "The thin-cap fibroatheroma: a type of vulnerable plaque: the major precursor lesion to acute coronary syndromes." *Curr Opin Cardiol.* **16**(5):285-292.

33. Langheinrich, A.C., Bohle, R.M., Greschus, S., Hackstein, N., Walker, G., von Gerlach, S., Rau, W.S., Holschermann, H. (2004) "Atherosclerotic lesions at

micro CT: feasibility for analysis of coronary artery wall in autopsy specimens." *Radiology.* **231**:675–681.

34. Lee, R.T, Grodzinsky, A.J., Frank, E.H., Kamm R.D., and Schoen F.J. (1991) "Structure-dependent dynamic mechanical behavior of fibrous caps from human atherosclerotic plaques." *Circulation* **83:** 1764-1770.

35. Lee, R.T., Loree, H.M., Cheng, G.C., Lieberman, E.H., Jaramillo, N., Schoen, F.J. (1993) "Computational structural analysis based on intravascular ultrasound imaging before *in vitro* angioplasty : prediction of plaque fracture locations." *J Am Coll Cardiol.* **21:** 777-782.

36. Lendon, C.L., Davies, M.J., Born, G.V., Richardson, P.D. (1991) "Atherosclerotic plaque caps are locally weakened when macrophages density is increased." *Atherosclerosis* **87:** 87-90.

37. Libby, P. (1995) "Molecular bases of the acute coronary syndromes." *Circulation* **91**:2844-2850.

38. Libby, P. (2001) "Current Concepts of the Pathogenesis of the Acute Coronary Syndromes." *Circulation* **104:** 365.

39. Little, W.C.. (1990) "Angiographic assessment of the culprit coronary artery lesion before acute myocardial infarction." *Am J Cardiol.* **66:** 44G-47G.

40. Llodra, J., Angeli, V., Liu, J., Trogan, E., Fisher, E. A., and Randolph, G. J. (2004) "Emigration of monocyte-derived cells from atherosclerotic lesions characterizes regressive, but not progressive, plaques." *Proc Natl Acad Sci U S A.* **101**:11779-11784.

41. Loree, H.M., Kamm, R.D., Stringfellow, R.G., Lee, R. (1992) "Effects of fibrous cap thickness on peak circumferential stress in model atherosclerotic vessels." *Circ Res*. **71:** 850-858.

42. Maehara, A., Mintz, G.S., Bui, A.B., Walter, O.R., Castagna, M.T., Canos, D., Pichard, A.D., Satler, L.F., Waksman, R., Suddath, W.O., Laird, J.R. Jr, Kent, K.M., Weissman, N.J. (2002) "Morphologic and angiographic features of coronary plaque rupture detected by intravascular ultrasound." *J Am Coll Cardiol.* **40**:904-910.

43. Moore, M.P., Spencer, T., Salter, D.M., Kearney, P.P., Shaw, T.R., Starkey, I.R., Fitzgerald, P.J., Erbel, R., Lange, A., McDicken, N.W. (1998) "Characterisation of coronary atherosclerotic morphology by spectral analysis of radiofrequency signal: in vitro intravascular ultrasound study with histological and radiological validation." *Heart* **79**:459–467.

44. Muller, J.E., Tofler, G.H. (1992) "Triggering and hourly variation of onset of arterial thrombosis." *Ann Epidemiol.* **2**: 393–405.

45. Nakahara, I., Tsuchida, E., Takezaki, J., Kodama, M. (1979) "Recent Research on Mechanical Behavior of Solids" ed. Miyamoto, H. (Univ of Tokyo Press, Tokyo), pp 119–138.

46. Nakamura, M., Nishikawa, H., Mukai, S., *et al*. (2001) "Impact of coronary artery remodeling on clinical presentation of coronary artery disease: An intravascular ultrasound study". *J Am Coll Cardiol.* **37:** 63-69.

47. Nakashima, Y., Plump, A.S., Raines, E.W., Breslow, J.L., Ross, R. (1994) ApoE-deficient mice develop lesions of all phases of atherosclerosis throughout the arterial tree. *Arterioscler Thromb.* **14**(1):133-140.

48. Ohayon, J., Finet, G., Treyve, F., Rioufol, G. and Dubreuil, O. (2005) "A three-dimensional finite element analysis of stress distribution in a coronary atherosclerotic plaque: *In-vivo* prediction of plaque rupture location." Biomechanics Applied to Computer Assisted Surgery: 225-241 ISBN: 81-308-0031-4 Editor: Yohan Payan.

49. Ohayon, J., Finet, G., Gharib, A.M., Herzka, D.A., Tracqui, P., Heroux, J., Rioufol, G., Kotys, M.S., Elagha, A., Pettigrew, R.I. (2008) "Necrotic core thickness and positive arterial remodeling index: emergent biomechanical factors for evaluating the risk of plaque rupture." *Am J Physiol Heart Circ Physiol.* **295**(2):H717-727.

50. Plump, A.S., Smith, J.D., Hayek, T., Aalto-Setala, K., Walsh, A., Verstuyft, J.G., Rubin, E.M., Breslow, J.L. (1992) "Severe hypercholesterolemia and atherosclerosis in apolipoprotein E-deficient mice created by homologous recombination in ES cells." *Cell.* **71**(2):343-353.

51. Rattazzi, M., Bennett, B. J., Bea, F., Kirk, E. A., Ricks, J. L., Speer, M., Schwartz, S. M., Giachelli, C. M., and Rosenfeld, M. E. (2005) "Calcification of advanced atherosclerotic lesions in the innominate arteries of ApoE-deficient mice: potential role of chondrocyte-like cells." *Arterioscler Thromb Vasc Biol **25**:* 1420-1425.

52. Rasheed, Q., Nair, R., Sheehan, H., et al. (1994) "Correlation of intracoronary ultrasound plaque characteristics in atherosclerotic coronary artery disease patients with clinical variables." *Am J Cardiol.* **73:** 753–758.

53. Reddick, R.L., Zhang, S.H., Maeda, N. (1994) "Atherosclerosis in mice lacking apo E. Evaluation of lesional development and progression." *Arterioscler Thromb.* **14**(1):141-147.

54. Richardson, P.D., Davies, M.J., Born, G.V.R. (1989) "Influence of plaque configuration and stress distribution on fissuring of coronary atherosclerotic plaques." *Lancet* **2**:941-944.

55. Rosenfeld, M. E., Polinsky, P., Virmani, R., Kauser, K., Rubanyi, G., and Schwartz, S. M. (2000) "Advanced atherosclerotic lesions in the innominate artery of the ApoE knockout mouse." *Arterioscler Thromb Vasc Biol **20:*** 2587-2592.

56. Schoenhagen, P., Ziada, K.M., Kapadia, S.R., Crowe, T.D., Nissen, S.E., Tuzcu, E.M. (2000) "Extent and direction of arterial remodeling in stable versus unstable coronary syndromes : an intravascular ultrasound study." *Circulation.* **101**(6):598-603.

57. Stary, H.C. (2001) "The development of calcium deposits in atherosclerotic lesions and their persistence after lipid regression." *Am J Cardiol* **88:** 16E–19E.

58. Stary, H.C. (2003) *Atlas of Atherosclerosis Progression and Regression* (Parthenon, London_New York).

59. Sundaram, K., Nishimura, R., Senn, J., Youssef, R.F., London, S.D., Reddy, S.V. (2007) "RANK ligand signaling modulates the matrix metalloproteinase-9 gene expression during osteoclast differentiation." *Exp Cell Res*. **313**(1):168-78.

60. Tanaka A, Imanishi T, Kitabata H, Kubo T, Takarada S, Tanimoto T, Kuroi A, Tsujioka H, Ikejima H, Ueno S, Kataiwa H, Okouchi K, Kashiwaghi M, Matsumoto H, Takemoto K, Nakamura N, Hirata K, Mizukoshi M, Akasaka T. (2008) "Morphology of exertion-triggered plaque rupture in patients with acute coronary syndrome: an optical coherence tomography study." *Circulation.* **118**(23):2368-73.

61. Tang, D., Yang, C., Zheng, J., Woodard, O. K., Sicard, G. A., Saffitz, J. E., and Yuan, C. (2004) 3D MRI-Based Multi-Component FSI Models for Atherosclerotic Plaques: A 3-D FSI model. *Ann. Biomed. Eng*., **32**(7): 947–960.

62. Tang, D, Yang, C, Zheng, J, Woodard, PK, Saffitz, JE, Petruccelli, JD, Sicard, GA & Yuan, C. (2005) "Local maximal stress hypothesis and computational plaque vulnerability index for atherosclerotic plaque assessment." *Ann Biomed Eng* **33**: 1789–1801.

63. Tsuchida, E., Togawa, S., Nakahara, I. (1976) *Bull JSME* **19**:838–848.

64. Tsutsui, S., Saito, K. 1973. Proc Japan Natl Congr Appl Mech. 23:547–560.

65. Varnava, A.M., Mills, P.G., Davies, M.J. (2002) "Relationship between coronary artery remodeling and plaque vulnerability." *Circulation.* **105**(8):939-943.

66. Virmani, R., Kolodgie, F.D., Burke, A.P., et al. (2000) "Lessons from sudden coronary death: a comprehensive morphological classification scheme for atherosclerotic lesions." *Arterioscler Thromb Vasc Biol* **20**: 1262–75.

67. Virmani, R., Burke, A.P., Kolodgie, F.D., Farb, A. (2003) "Pathology of the thin-cap fibroatheroma: a type of vulnerable plaque." *J Interv Cardiol* **16:** 267-272.

68. Vengrenyuk, Y., Carlier, S., Xanthos, S., Cardoso, L., Ganatos, P., Virmani, R., Einav, S., Gilchrist, L., and Weinbaum, S. (2006) "A hypothesis for vulnerable plaque rupture due to stress-induced debonding around cellular microcalcifications in thin fibrous caps." *PNAS* **103**(40): 14678-14683.

69. Vengrenyuk, Y., Cardoso, L., Weinbaum, S. (2008) "Micro-CT based analysis of a new paradigm for vulnerable plaque rupture: cellular microcalcifications in fibrous caps." *Mol Cell Biomech.* **5**(1):37-47.

70. Williams, H., Johnson, J.L., Carson, K.G., Jackson, C.L. (2002) "Characteristics of intact and ruptured atherosclerotic plaques in brachiocephalic arteries of apolipoprotein E knockout mice." *Arterioscler Thromb Vasc Biol.* **22**(5):788-792.

71. Yilmaz, A., Reiss, C., Tantawi, O., Weng, A., Stumpf, C., Raaz, D., Ludwig, J., Berger, T., Steinkasserer, A., Daniel, W.G., Garlichs, C.D. (2004) "HMG-CoA reductase inhibitors suppress maturation of human dendritic cells: new implications for atherosclerosis." *Atherosclerosis* **172**:85–93.

72. Zhang, S.H., Reddick, R.L., Piedrahita, J.A., Maeda, N. (1992) "Spontaneous hypercholesterolemia and arterial lesions in mice lacking apolipoprotein E." *Science.* **258**(5081):468-471.